Development of Internal Magnetic Probe Array with Dual Sensors in Versatile Experiment Spherical Torus (VEST)

VEST에서의 이중 감지기 내부 자기장

탐침 시스템 개발

2013 년 8 월

서울대학교 대학원

에너지시스템공학부 원자핵공학전공

양 정 훈

Abstract

Development of Internal Magnetic Probe Array with Dual Sensors in Versatile Experiment Spherical Torus (VEST)

Yang Jeong-hun

Department of Engineering

The Graduate School

Seoul National University

The internal magnetic probe array is developed to measure the magnetic structure of Versatile Experiment Spherical Torus (VEST) during the startup phase including the null formation and plasma merging. Two types of sensors, Hall sensor and chip inductor, are used to measure both slow and fast varying magnetic fields. Since the size of both sensors is small, the magnetic probe array may be inserted to plasma without changing the plasma parameters significantly.

A chip inductor with ceramic core and an integrated Hall sensor are selected as the magnetic sensors. The minimum measurable magnetic field above the noise level and the frequency response are considered in the selection process. Then the target magnetic structure is assessed to specify the 25 measurement positions that satisfy the engineering constraints and minimize the interpolation errors. The magnetic sensors are then soldered onto the printed circuit board specially designed to measure all three dimensions of magnetic field. Various means of electromagnetic interference is shielded, and especially the copper braided wire is used for shielding of electron cyclotron resonance frequency microwave to the noise level of 7 G. Thermal load from the plasma stored energy is calculated in the course of designing the fused silica tube. The negligible temperature rise of 0.2 ℃ is predicted, and therefore no active cooling channel is adopted.

Helmholtz coil is constructed to absolutely calibrate the magnetic sensors after they are mounted on the printed circuit board. The power required for generation of 100 G magnetic field is provided by an audio amplifier. For Hall sensors, the calibrated sensitivity is 13 V/T and the calibrated frequency response is 0.03 to 10 kHz. For chip inductors, the sensitivity is 7.52 V/T and the frequency response is 0.1 to 50 kHz. The phase shift in both sensors is negligible even with the copper braided wire shielding, since the wire is equivalent to extremely thin metal sheet.

The calibrated magnetic sensors are installed in VEST lower chamber. The misalignment of the sensors is calibrated in-situ using the toroidal field of VEST. The radial measurement position is also calibrated using the toroidal field. It is notable that these methods can be suggested because the toroidal field can be measured accurately using the internal magnetic probe array.

Test measurements on vacuum field have been done. The comparison with the predicted vacuum field shows good agreement in most locations. However, measured field near the edge showed disagreement which is probably due to the eddy current that is difficult to be accurately accounted for. Another test on the artificial field generated by numerically prescribed plasma current is done to test the feasibility of internal magnetic probe array in the measurement of plasma current density profiles. The current density profile that produces vertical magnetic field gradient scale length of 3 cm is found to be reconstructed with less than 2 % error by using current design of the probe array.

Improvement in the flux function reconstruction may be done by combining the internal magnetic probe array with other magnetic measurements such as flux loops and external pickup coils. Also the shorter interval between sensors that reconstruct a wider range of plasma shapes may be needed. Based on these experiences, an internal magnetic probe array in the middle chamber of VEST will be constructed in the near future.

Contents

iii

List of Tables

List of Figures

Chapter 1 Introduction

1.1   Versatile Experiment Spherical Torus (VEST)

Nuclear fusion is a promising source of energy. The leading concept in the study of the fusion energy is *tokamak*, in which the high-energy charged particles are trapped within a torus-shaped device by magnetic fields. Spherical tokamak (ST) is a branch of tokamak that features low aspect ratio (ratio of major radius to minor radius) and high plasma beta (ratio of plasma pressure to magnetic pressure). [1] Due to the high performance and small size, ST is an attractive candidate for the future fusion reactor. The major drawback of ST, however, is that a space to accommodate a central solenoid is limited, and therefore the startup of ST is rather difficult.

Versatile Experiment Spherical Torus (VEST) is an ST to study such an issue. It features a low aspect ratio of 1.3 with major radius 0.4 m and minor radius 0.3 m. Inspired by double null merging startup scheme explored in START and MAST, [2, 3] a pair of *partial solenoids* are used for generation of small plasmas in the vertical ends of the vacuum chamber. The small plasmas in the upper and lower chambers may then merge in the middle chamber. [4] Since the partial solenoids can only supply a limited solenoid flux, the pre-ionization is done by the electron cyclotron resonance heating. The toroidal field is designed to be 0.1T on axis and the initial plasma current is targeted at 30kA.

This thesis deals with one of the magnetic measurement systems in VEST to contribute to the research on the ST for the realization of the fusion energy.
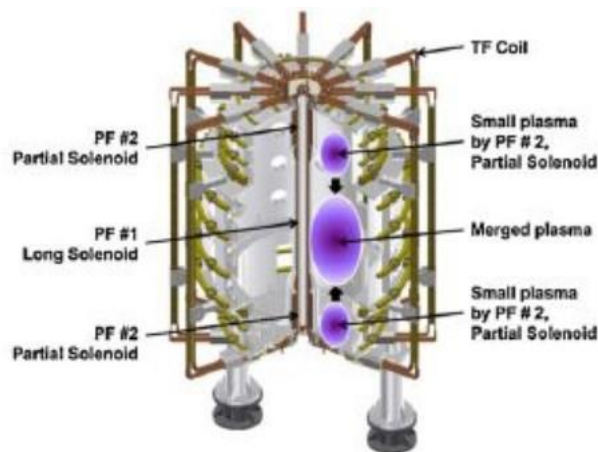
Figure 1.1 Schematic of VEST and startup scheme using partial solenoid [4]

1.2 Review of Current Density Profile Measurement

Tokamak confinement is achieved by toroidal and poloidal fields. The fields are generated by the current driven through the external coils and the plasma. To predict and improve the confinement, the currents should be measured accurately. Therefore the radial distribution of plasma current density, or plasma current density profile, has been an important subject in tokamak plasma diagnostics.

Equilibrium reconstruction is the basic method to obtain the current density profile in most of the tokamaks. In a tokamak geometry, a relation pertains between the current density profile and the flux function as in the following equation:

$$\Delta^* \Psi_\theta = -2\pi r \mu_0 J_\varphi \qquad\qquad (1.1)$$

Here, Ψ_θ is the poloidal flux function, r the major radius and J_φ the toroidal current density (Δ^* is the elliptic operator). Using Equation 1.1, the last closed flux surface can be derived by searching for the best fits with magnetic measurements. Plasma current can be modelled by a certain distribution function or distribution of multiple filaments, [5] or by a distribution of weighted finite elements, [6] as shown in Figure 1.2. However, only the global parameters of the plasma current density profile can be determined when the measurement is restricted to the outside of the plasma. [7]
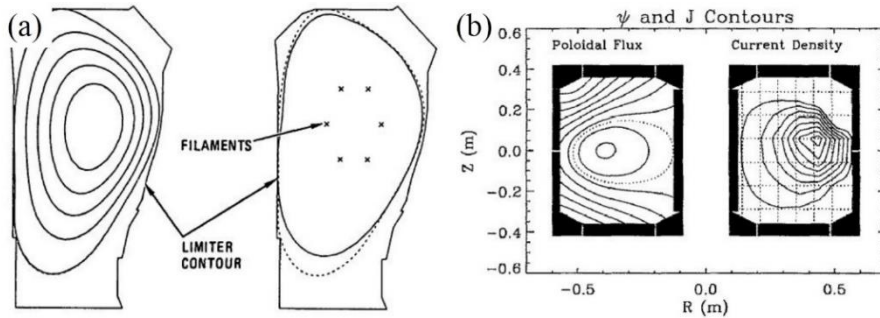
Figure 1.2 Equilibrium reconstruction of poloidal flux and current density using:
(a) Current distribution model (left) and multiple filament model (right) used in DIII-D [5].
(b) Finite element weighted current density model used in CDX-U [6].

To obtain the current density profile inside the plasma, additional magneto-hydrodynamic (MHD) constraints are required. Kinetic profile (radial distribution of electron density or temperature) measurement can provide such constraint. [7] If possible, internal magnetic field (field inside the plasma) measurement is more direct way of reconstructing the current density profile. Two non-perturbing methods for the internal magnetic field measurement are discussed in the next paragraph, and shown in Figure 1.3.
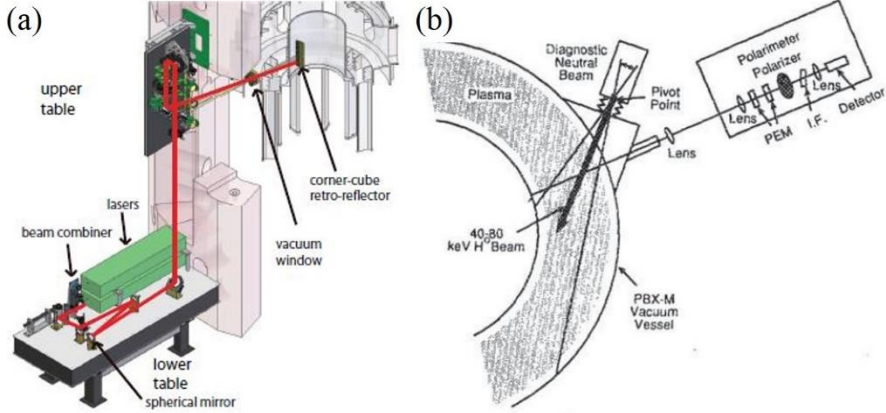
Figure 1.3 Illustration of Faraday rotation and motional Stark effect in tokamaks.
(a) Faraday rotation measurement setup in Alcator C-MOD [8].
(b) Motional Stark effect measurement setup in PBX-m [11].

Faraday rotation is a non-perturbing measurement that yields a line-averaged magnetic field as in the following relation:

$$\alpha_{pl} \sim \lambda^2 \int n_e \vec{B} \cdot \vec{dl} \qquad (1.2)$$

Here, α_{pl} is the rotation angle, λ the wavelength, and vector *dl* the length element along the path of an incident laser beam. To obtain the local magnetic field, the measured α_{pl} must go through the Abel inversion, which is a rather complicated process. Moreover, the technology to reduce the noise in wave modulation in tokamaks is still developing. Therefore Faraday rotation is used in tokamaks where the need for the non-perturbing measurement outweigh the technical difficulties, such as Alcator C-MOD and HL-2A [8, 9]. *Motional Stark effect* (MSE) is also a non-perturbing method, and the polarized radiation from a diagnostic neutral beam is measured. Then the pitch angle of **B** can be determined from the effective electric field $\mathbf{E}_{eff} = \mathbf{v}_{beam} \times \mathbf{B}$, where $\mathbf{v}_{beam}$ is the beam velocity vector. For small tokamaks, however, MSE is an advanced and expensive method requiring diagnostic neutral beam. Therefore, MSE is adopted in large or mid-sized tokamaks

3

such as DIII-D and PBX-M [10, 11].

The non-perturbing methods described in the previous paragraph befit the large and mid-sized tokamaks. In small tokamaks operating at relatively low plasma density and temperature, on the other hand, magnetic probe can be inserted into the plasma. Two major issues of the internal magnetic probe are: (1) the heat flux from plasma may damage the probe, and (2) the physical presence of probe may perturb the plasma. Once the effects are predicted, however, internal magnetic probe can be extremely valuable since it provides the direct measurement of the local current density with excellent time resolution. [12] Details of the inserted probe are discussed in the separate section in chapter 2.

1.3   Motivation and Objectives

In order to measure plasma parameters, the VEST magnetic diagnostic system is composed of inner and outer Rogowski coils, flux loops, magnetic field probes and internal magnetic probe array. [13] Other diagnostics include the movable triple Langmuir probe and single channel interferometer for kinetic profiles measurement (electron density and temperature) and the 20 kHz fast CCD camera to monitor the plasma evolution. Soft X-ray and Thomson scattering systems are currently under development. Among those diagnostics, internal magnetic probe *array* measures the magnetic field *structure* inside the plasma.

For VEST, the assessment of the field null formation is important in generation of the small plasma using the partial solenoids. However, the vacuum field configuration is difficult to predict due to the thick conducting walls of vacuum vessel where significant eddy currents may set in. Therefore the internal magnetic probes should provide the information on the field null formation that can lead to a successful startup. Since vacuum field evolution is in the time scale of milliseconds, a magnetic sensor compatible with low frequency are required.

Another special feature of the VEST magnetic field structure is the merging of plasma. Plasma boundary moves during the merging, and in the process the magnetic fields can reconnect due to the finite resistivity. Such phenomena may be monitored directly by the internal magnetic probes, which may provide a reference point and improve the theoretical models. Typical time resolution of microseconds is expected for the measurement of this characteristic VEST magnetic field evolution.

This thesis is motivated by the need of the internal magnetic probe array in VEST. To meet the aforementioned VEST-specific requirements, two types of sensors – Hall sensors and chip inductors – that feature different frequency responses are used simultaneously. Despite the increased number of accommodated sensors, the size of internal magnetic probe array should remain small. Therefore the objectives of this thesis can be summarized in three points:

> **(1)** Design and fabricate the internal magnetic probe array using both Hall sensors and chip inductors while maintaining small size,
>
> **(2)** Calibrate the constructed internal magnetic probe array for the use in VEST, and
>
> **(3)** Document the operational details and limits of the internal magnetic probe array.

1.4   Thesis Outline

In this thesis, developing process of internal magnetic probe array is explored, with consideration of the important engineering constraints imposed for the VEST.

In chapter 2, the literature on the previous work on internal magnetic probe is introduced. Then the theoretical aspects, such as the principle of the sensors and the derivation of plasma parameters from the measurement, are presented.

In chapter 3, the overall system design is described. Requirements for the internal magnetic probe array in VEST are stated, before the specifications of the design parameters are determined. Additional design features, such as thermal shielding and electromagnetic interference compensation are described.

In chapter 4, the calibration results of the fabricated internal magnetic probe array using Helmholtz coil system is presented. Effects of electromagnetic shielding components on signal distortion due to the skin effect are also presented.

In chapter 5, the process of system assembly and installation on VEST is depicted. Then the in-situ calibration schemes using toroidal field coils of the VEST that allows correction of misalignment of the sensors in angle and position are suggested.

In chapter 6, two test experiments are presented. First, the results from vacuum field measurement using one of the poloidal field coils of VEST are presented. Then the phantom plasma field is introduced to examine the possible limitations in the reconstruction of real plasma current density profiles using the internal magnetic probe array in the future.

In chapter 7, thesis will be summarized with a conclusive statement on the development of internal magnetic probe array. Future work is also discussed in this chapter.

Chapter 2 Theoretical Backgrounds

2.1   Previous Work on Magnetic Probe Array

The Internal magnetic probe was first used in 1971 at Australia by D.L. Bowers and others, in attempt to determine the evolution of current density profile inside a θ-Z pinch, in the study of the disruptive instabilities [14]. A single magnetic probe was inserted by shot-to-shot basis into the different radial positions. Two important problems were the time resolution being limited due to the statistical fluctuations of the instabilities, and the difficulty in prediction of the systematic perturbation of the progressive introduction of magnetic probe [15].

I.H. Hutchinson worked on the disruptive instability in LT-3 tokamak with an array of magnetic probes permanently inserted in the plasma, in order to overcome the limitations discussed on the previous work [15]. In this work, pickup coils recorded magnetic fields at 18 points 0.5 cm apart to a distance z = 3.5 cm from the vessel minor axis. Insertion to closer than 3 cm led to completely perturbed plasma behavior, but otherwise the field by the perturbed discharge was measured accurately. Figure 2.1 shows the results. The magnetic field data from measurement was fitted to a polynomial and a current density profile was deduced from the polynomial. The disruptive relaxation of the current density profile within a few microseconds was successfully measured by using the pickup coils.
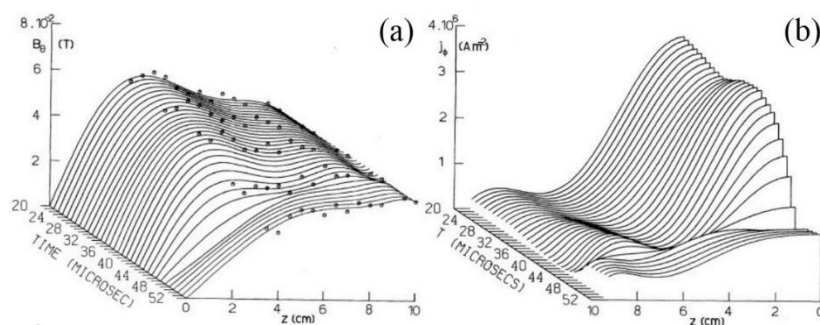
Figure 2.1 (a) Measured evolution of poloidal magnetic field and (b) toroidal current profile at LT-3. Note the minor axis positions (z = 0 cm) in both figures. Positions of measurements are marked with circle in (a), and the fitted polynomials are shown in lines.

The results of I.H. Hutchinson was reproduced in several tokamaks such as TOSCA, TNT-A, MINIMAK and TORTUS [16]. In TORTUS, 16 pickup coils were inserted to the minor axis, as shown in Figure 2.2. The small tokamaks adopted pickup coil arrays to study the microsecond-scale MHD instabilities.
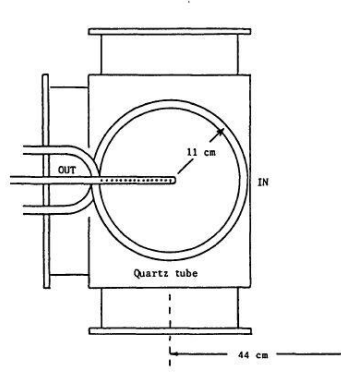
Figure 2.2 Schematic drawing of internal magnetic probe array in TORTUS [16].

Recent progress in the technique of manufacturing pickup coils led to the development of a commercialized pickup coil, or chip inductors. Inspired by the advent of the chip inductor, C.A. Romero-Talamás and others worked on the measurement of magnetic field configuration at 20 points of Caltech Spheromak [17]. This work also focused on the events in the microsecond-scale.
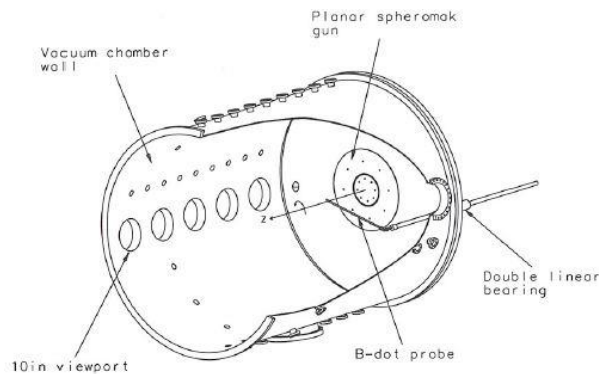
Figure 2.3 Schematic drawing of internal magnetic probe array in Caltech Spheromak [17].

I. Ďuran and others worked on the pioneering research using Hall sensors to measure the MHD activity preceding disruptions or sawteeth in the scrape-off-layer of TEXTOR tokamak [18]. Three Hall sensors measured each directions of the magnetic field at a single position 4cm outside the last closed flux surface. However, the Hall sensor was large and the probe size was 3 cm diameter, so the Hall sensor could not be inserted into the plasma core. The sensors measured MHD activities in a frequency band from 300 Hz to 10 kHz to study disruptions, sawteeth and Radiative Improved (RI) mode. In Figure 2.4, measured magnetic fields show disruptive precursor at the frequency of 0.3 and 2 kHz and sawtooth precursor at the frequency of 5 to 10 kHz.
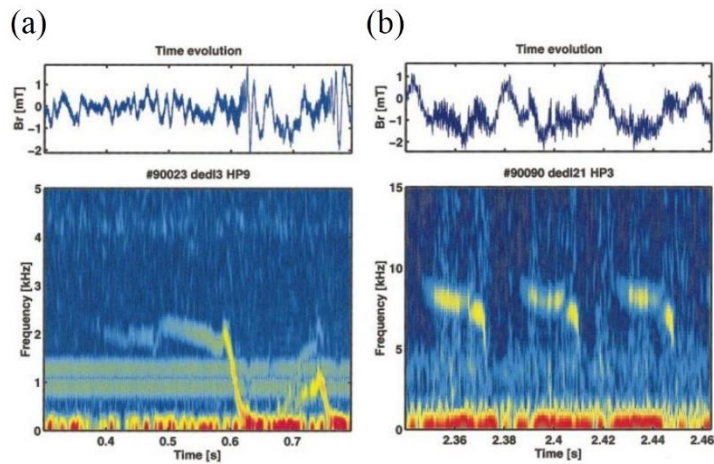
Figure 2.4 Results of experiments on (a) disruption and (b) sawtooth instability measured by Hall sensor. Colored panel is time-frequency plot by fast Fourier transform analysis. The measured magnetic fields are shown in the top panels [18].

Y. Liu and others expanded the idea of I. Ďuran in HBT-EP tokamak by inserting an array of 20 Hall sensors placed on a printed circuit board and positioned in the scrape-off-layer [19]. This work also explored the frequency range below 20 kHz, where the Edge Localized Mode (ELM) was activated.

Development of an advanced Hall sensor with smaller size and stabilized performance led to the plasma position measurement in CASTOR tokamak using a ring shaped array of 16 Hall sensors by I. Ďuran and others [20]. This work was focused on the movement of plasma within several 10 milliseconds. Another work of I. Ďuran investigated the prospects of steady state magnetic field measurement using another newly developed metallic Hall sensor [21]. The development of the Hall sensors is explained in Section 2.2.2 in more detail.

Previous work on magnetic probe array is summarized in terms of frequency in Table 2.1. It is noteworthy that largely two categories of magnetic probes were used. The pickup coil and chip inductor family measured faster events in the frequencies of larger than 1 kHz. On the other hand, Hall sensor measured slower events at the frequencies of smaller than 20 kHz.

Table 2.1 Frequency band of plasma properties and the sensors used for measurements

Frequency	100 kHz ↑	10 kHz	1 kHz ↓	Steady State
Property	Spheromak plasma evolution	MHD activity in tokamaks	Tokamak plasma evolution	ITER plasma evolution
Sensor	Chip inductor	Pickup coil Hall sensor	Hall sensor	Hall sensor

2.2 Principles of Magnetic Sensors

In order to measure both slow evolution of vacuum field and fast evolution of merging plasma magnetic field in VEST, both chip inductor and Hall sensor are used in the internal magnetic probe array. In this section, the principles of the sensors are reviewed, and the frequency response of each sensor is elaborated.

2.2.1 Chip Inductor

A changing magnetic field induces an electric field. Faraday's law is used to predict an electric field induced by magnetic field threading the surface of a loop of wires:

$$V = -NA\frac{\partial B}{\partial t}. \qquad (2.1)$$

Here, A is the area of the loop surface, B the surface-averaged magnetic field and N the number of wire turns. The product of turns and area NA in Equation 2.1 is called the *effective area* and is a common indicator of the sensitivity of an inductive coil.

Chip inductor is a commercialized inductive coil. When winding the coil by hand, the number of turns per unit length is limited and the area of the winding bobbin has to be big enough. However, factorized process allows extremely thin wires to be wound very compactly into a miniature bobbin. Moreover, the thin film conductor technology gives even more freedom in the chip inductor design.

Self-resonant frequency of any pickup coil is a frequency of induced voltage around which the inductor starts to act like a capacitor. This transition is due to the tendency of high frequency oscillating currents to flow at the surface rather than the core, or skin effect. The increased resistance blocks the current flow and the adjacent conductors see each other as a capacitive electrode. Therefore it is important to check that the self-resonant frequency is above the frequency to be measured by the chip inductor.

Normally an analog integrator is used to relate the voltage with magnetic field, rather than its time variation. With an integrator of time constant RC, Equation 2.1 is modified as follows

$$V = -\frac{NA}{RC}B \qquad (2.2)$$

Analog Integrator is an op amp application accommodating a grounded

positive input, a resistor to the negative input and a negative feedback loop equipped with a capacitor. Time constant of an analog integrator is a product of the resistance and capacitance by transfer function analysis that is not elaborated in this thesis. Another large resistor (Miller resistor) is often connected in parallel with the capacitor to allow the integration of slowly varying inputs. In addition to analog integrator, an amplifier is often used to control the signal intensity. Then the total gain of the integrator becomes a product of inverse of time constant and the amplification factor.

Chip inductor basically measures the time variation of magnetic field. This means for steady fields the coil becomes ineffective unless it is moved across the spatial variation of the magnetic field. Moving the probe array along the tokamak is not practical, so chip inductor is not an attractive means for measurement of slowly changing magnetic fields. The low frequency threshold is determined by the rate of change of the magnetic field at which the output voltage is distinguishable from the noise level.

2.2.2   Hall Sensor

The Hall effect is first observed in 1879 by E. Hall. Detailed description of Hall effect is rather complicated, but in essence it can be interpreted as a Lorentz force acting on a charged particle moving across a magnetic field. A virtually solid state plasma such as semiconductor may host such an effect. Consider a slab with two pairs of conductor immersed in a magnetic field as depicted in Figure 2.5. Application of the Hall current I_H in y axis direction gives rise to a charge accumulation due to the Lorentz force in x by the magnetic field B in z. Thus the charge accumulation gives rise to the Hall voltage U_H in x axis direction. This relation is summarized as:

$$U_H = k_H I_H B \sin \alpha. \qquad (2.3)$$

Here, k_H is the Hall coefficient and α is the angle between the Hall current and the magnetic field.
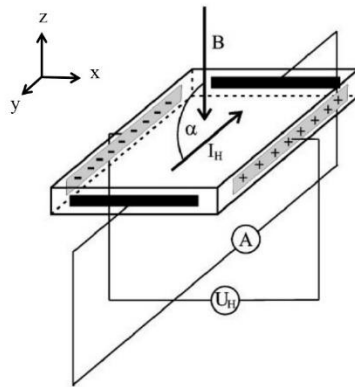
Figure 2.5 Illustration of Hall effect in N type semiconductor slab. Modified from [18].

Hall coefficient k_H is determined by the dimension and the material of the Hall sensor. The first Hall sensors used only a slab of semiconductor as shown in Figure 2.5, which yielded only a small Hall coefficient as a material. Therefore the Hall sensor had to be big in size to enhance the Hall voltage and improve signal to noise ratio. Later, the so-called *integrated* Hall sensor is developed. This advanced Hall sensor is cohabited by an integrated circuit inside a small box. The integrated circuit amplifies the Hall voltage, allowing the Hall sensor to be small. The other important role of the integrated circuit is stabilization of the performance.

The Hall coefficient of a semiconductor based Hall sensor is susceptible to the changing ambient temperature. Therefore the performance of the first Hall sensors was significantly dependent on the weather, climate and seasons. The circuitry in the advanced Hall sensor stabilizes this fluctuation due to temperature by controlling the Hall current. Then the drift of Hall voltage with temperature is greatly reduced. Characteristic response of this circuitry is that when supplied with a voltage V, the quiescent output voltage for zero magnetic field, or the offset, is $0.5V$.

A metallic Hall sensor is being developed for use in ITER. The susceptibility to the ambient temperature of Hall sensor is less significant when based on metals rather than semiconductors. With neutron activation tests on various candidate materials and development of the integrated circuit to control the performance, the metallic Hall sensor may serve an important role in the future.

Hall sensor is built on a semiconductor where electron or electron hole moves by a finite speed. Therefore, the magnetic field changing too fast for the charge carriers to respond is not picked up by Hall sensor. Typically an oscillation faster

than 20 kHz cannot be measured reliably.

2.3   Magnetic Field Analyses from Maxwell's Equation

Maxwell's equations specify the divergence and curl of electric and magnetic fields. In this section, Faraday's law and another two of the Maxwell's equations regarding magnetic field are examined in axisymmetric toroidal geometry. The axisymmetric toroidal geometry and poloidal flux function is introduced. This knowledge leads to progressive treatment of measured local magnetic field to calculate the local current density and electric field.

Axisymmetric toroidal geometry is best represented by a branch of three dimensional cylindrical coordinates system (r, φ, z) where the axis $r = 0$ is the rotational axis of the tokamak. It can be stated that in what follows, r denotes the radial position, φ the toroidal angle, and z the vertical position. The condition where a quantity is toroidally axisymmetric means the quantity has no dependency on φ, hence $\partial/\partial \varphi = 0$.
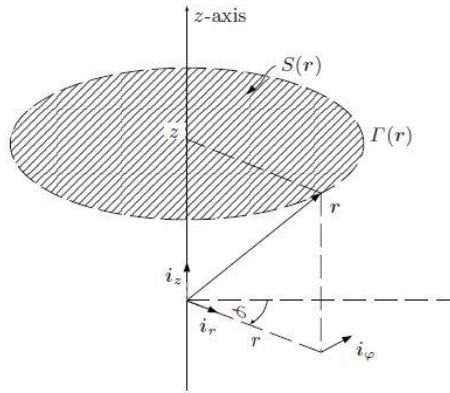
Figure 2.6 Illustration of axisymmetric toroidal geometry. Here, $\Gamma(r)$ denotes the circumference drawn by the rotation of the point r, and S(r) denotes the surface enclosed by the edge $\Gamma(r)$ [22].

Poloidal flux function is a convenient tool to represent the magnetic structure, since the function is a scalar, unlike the poloidal magnetic field, a vector. The analogy of a fluid flux is applied here and the poloidal flux function is defined as follows:

$$\Psi(r) \equiv \int_{S(r)} \vec{B} \cdot d\vec{S} \qquad (2.4)$$

14

$$\Psi(r) = \int_0^r \int_0^{2\pi} B_z(\rho, z)\rho\, d\rho\, d\varphi$$

$$= 2\pi \int_0^r \rho B_z(\rho, z)\, d\rho \qquad\qquad\qquad (2.4a)$$

Here the unit is in SI, and flux function is in Weber. In many cases, the flux function is in Weber per radians, in which case one need only to divide the relation by 2π. Note that ρ in Equation 2.4a is an integration coefficient equivalent to r. See Figure 2.6 for the notations.

Divergence of the magnetic field is zero, and this statement is often called a Gauss's law of magnetics.

$$\nabla \cdot \vec{B} = 0 \qquad\qquad\qquad (2.5)$$

$$\frac{1}{r}\frac{\partial}{\partial r}r B_r + \frac{\partial}{\partial z}B_z = 0 \qquad\qquad\qquad (2.5a)$$

Differentiation of Equation 2.4a in r gives the relation between B_z and the derivative of the flux function. Taking into account the Equation 2.5a, and differentiating the Equation 2.4a in r, the following relation can be derived.

$$\frac{\partial}{\partial r}\Psi = r B_z \text{ and } \frac{\partial}{\partial z}\Psi = -r B_r \qquad\qquad\qquad (2.6)$$

This equation relates the radial and vertical magnetic field with poloidal flux function. It means that if vertical field is known, flux function and radial field can be derived by simple integration and differentiation. This is noteworthy because the engineering constraints often disallow the measurement of both radial and vertical magnetic fields using internal magnetic probe.

Curl of the magnetic field is proportional to the local current density. Assuming the magnetostatic situation, displacement current term of the Ampère's law can be neglected.

$$\nabla \times \vec{B} = \mu_0 J \qquad\qquad\qquad (2.7)$$

$$\frac{\partial}{\partial z}B_r - \frac{\partial}{\partial r}B_z = \mu_0 J_\varphi \qquad\qquad\qquad (2.7a)$$

Toroidal current density can be obtained from radial and vertical magnetic fields as shown in Equation 2.7a.

Faraday's law written with notations based on Figure 2.6 is rewritten as follows.

15

$$\oint_{\Gamma(r)} \vec{E} \cdot d\vec{l} = -\frac{\partial}{\partial t} \int_{S(r)} \vec{B} \cdot d\vec{S} \qquad (2.8)$$

Left hand side of this equation is toroidal electric field multiplied by 2π. (See Figure 2.6) Using the definition of poloidal flux function (Equation 2.4) it can be obtained that:

$$E_\varphi = -\frac{1}{r}\frac{\partial}{\partial t}\Psi \qquad (2.9)$$

Another important relation can be identified with Equation 2.9, that toroidal electric field can be derived by differentiation of poloidal flux function in time.

Equations 2.6, 2.7a and 2.9 provide the working relations on internal magnetic probe array measurement. Mere measurement of a local vertical magnetic field leads to calculation of the local poloidal flux function and radial magnetic field by Equation 2.6. Then the toroidal current density at the position can be determined by Equation 2.7a, and the toroidal electric field at the position can be determined by Equation 2.9.

Chapter 3 Overall Systems Design

3.1   Design Requirements

Issues on the design of internal magnetic probe array will be clarified once the design requirements are specified. In this section, the design requirements imposed in VEST are addressed.

The target magnetic structure can be derived from the poloidal flux function that satisfies Equation 1.1, for a given current density driven through the poloidal field coils and eddy currents in the vacuum vessel walls.

$$\Delta^* \Psi_\theta = -2\pi r \mu_0 J_\varphi \qquad (1.1)$$

The Typical poloidal field coil current swing down in VEST is within 10 ms, and the field evolution due to this driving current is in the scale of 0.01 T (100 G), so the variation of magnetic field is 1 T/s. Noise from electronics used to accompany the probe array is assumed to be 5 mV but may vary with conditions The noise levels will be described in the relevant sections in more detail.

The measured magnetic field is first interpolated. If the gradient scale length of magnetic fields too large or too small for the interpolation grid, the interpolation error becomes significant. The magnetic field gradient scale length is often approximated by plasma minor radius. Visual observation of the VEST plasma during a discharge by fast CCD camera showed a plasma size of 0.1 m (10 cm) in the upper and lower chambers. Search for an optimized spatial resolution regarding the interpolation error is discussed in section 3.2.2.

Electromagnetic interference is a major noise source for any electronics. In VEST, the wave energy coupling is dominant among the various means of interference, due to the microwave injection for the pre-ionization. The electron cyclotron resonance frequency wave oscillates in 2.45 GHz to match the electron resonance condition at the toroidal magnetic field of 875 G near the magnetic axis.

Heat load from plasma of VEST can be calculated from the assumption that plasma stored energy is dissipated to the internal probe. Stored energy is calculated for plasma density of 1×10^{18} m^{-3} and temperature 30 eV, based on the measurement by triple probe during the initial plasma experiments. Ion temperature is considered to be negligible at the initial phase of VEST operation. Plasma is assumed to be limited within a volume of rectangular cross section 0.4 m wide and 0.6 m high at upper/middle chamber and 0.7 m wide and 1.2 m high at middle chamber. Minor

axis position at $r = 0.4$ m is assumed. Then the stored energy is:

$$W_{stored} = P_{\text{plasma}}V = n_e T_e V \qquad (3.1)$$

Here, W_{stored} is the plasma stored energy, P_{plasma} the plasma pressure, V the plasma volume, and n_e and T_e are the electron density and temperature respectively. The stored energy is 15.9 J. Then the heat flux can be calculated once the surface is determined, which will be discussed more in section 3.4.

3.2 System Specifications

3.2.1 Sensor Selection

The chip inductor Coilcraft Ⓒ 1812CS-XGLC is selected. This sensor features the largest effective area among the chip inductor models with same size and produced by Coilcraft. The footprint dimensions are 4.95 mm × 3.81 mm and the height is 3.43 mm. The effective area provided by the manufacturer is 8.18 cm^2. Minimum measurable magnetic field is determined by the integrator gain and noise level. For an assumed noise level of 5 mV, the use of analog integrator of 1 ms time constant and additional gain of 20 (total gain of 20000) yields the minimum measurable magnetic field of 3.06 G. Without integrator, the minimum field variation of 6.1 T/s can be picked up beyond the noise level of 5 mV.

Self-resonant frequency of 1812CS-XGLC is 20 MHZ with tolerance of 2 %, which is much higher than the frequency of interest in many tokamak research. The dc resistance is 13.5 Ω with 145 mA dc current limit, and the inductance is 33 μH for frequencies up to 2.5 MHz. Since the capacitance component is negligible in the frequency band below MHz, L/R time may determine the high frequency limit of the chip inductor. The calculated L/R cutoff is 65 kHz.

The Hall sensor Winson Ⓒ WSH-135 is selected. This sensor features nominal sensitivity of 13 V/T, and the minimum measurable magnetic field is then 3.85 G based on the assumed noise level of 5 mV. Detailed analysis on the actual noise level is provided in Chapter 6. The sensitivity is the product of Hall current and Hall coefficient in Equation 2.3, assuming the angle $\alpha = 90°$. The footprint dimension of the Hall sensor is 4.00 mm × 3.15 mm and the height is 1.52 mm.

WSH-135 features a flat response to the frequencies from dc up to 23 kHz, according to the manufacturer. This sensor is an "integrated" Hall sensor that has a weak dependency to the ambient temperature with help of the accompanied circuits. Figure 3.1 shows the temperature drift of the output Hall voltage, tested and provided by the manufacturer. It can be inferred from Figure 3.1 that for temperature variation of 1 ℃, the drift of output voltage is 4.17 mV, and the error in magnetic field is 3.21 G. Therefore, if the temperature rise during a VEST operation is in the order of at least 1 ℃, an active cooling channel must be designed. However, the calculations to be explained in Section 3.4 show that such a cooling system is not required for the VEST internal magnetic probe array.

Output Voltage vs. Temperature
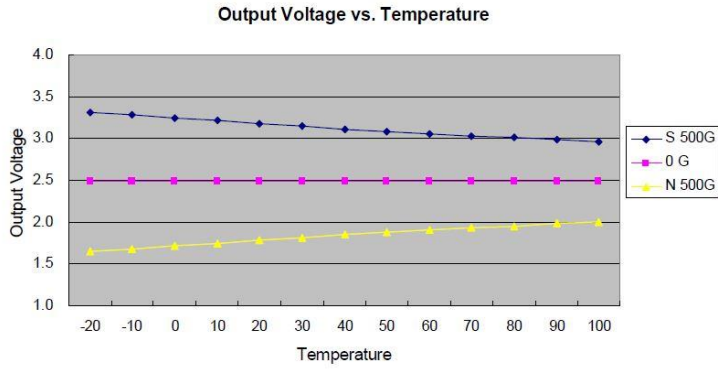
Figure 3.1 Characteristic curve of WSH-135 Hall sensor on output voltage with respect to ambient temperature [23].

3.2.2   Placing the Sensors

Magnetic fields at the positions in between two sensors can be obtained from an interpolation using the constraints given by the measurements at both ends. However, the interpolation introduces a numerical error that hinder the accurate representation of the spatial change of magnetic field between the sensors. In order to reduce this numerical error, the distance between sensors should be chosen with care. This section deals with the process of selecting sensor positions that introduce lowest interpolation error, with consideration of the physical constraints.

Internal magnetic probe array is to be installed on the already-made VEST vacuum vessel, which means the clearance for the sensor placement is limited. The finite size of an access port and the presence of poloidal field coils across the port limits the placement to the vertical positions from $z = -0.77$ m to $z = -1.05$ m. On the other hand, the radial clearance for the probes is the vacuum vessel boundary, from the center stack in the upper chamber that extends to $r = 0.15$ m to the outer wall placed at $r = 0.65$ m.

The interpolation error is assessed by changing the radial and vertical spacing between probes within the stated physical clearance. The target magnetic structure of VEST is used as a test field. Magnetic field at specific points are assumed to be measured. Then the magnetic fields at positions in between are interpolated. Cubic spline interpolation with natural end condition is used subsequently for both radial and vertical directions. The resulting average error is plotted in Figure 3.2.

20
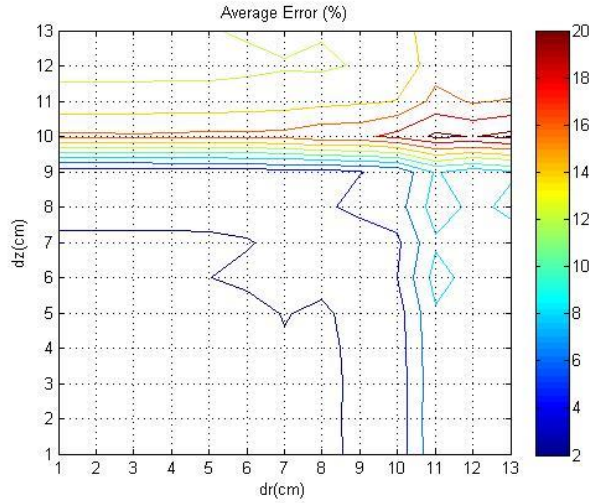
Figure 3.2 Contour plot of the average interpolation error for the radial and vertical sensor spacing values ranging from 1 cm to 13 cm.

Figure 3.2 shows the interpolation errors for various combinations of the radial and vertical sensor spacing. The error increases sharply when the vertical spacing (dz) becomes 10 cm rather than 9 cm. This means the interpolation using the grid size of 10 cm in vertical direction will introduce the average error of 20 %, whereas the grid size smaller than 9 cm will introduce that of only 5 %. A similar observation can be made by comparing the errors for the radial spacing (dr) of 10 and 11 cm. From the observations, it can be concluded that the interpolation grid size should be smaller than 9 cm vertically and smaller than 10 cm radially. Another way of interpreting the observation is that the gradient scale length of the vacuum field in VEST is 9 cm vertically and 10 cm radially, so that if sensors are placed with wider spacing then this will not be able to *capture* the spatial variation of the field.

Based on both the interpolation error analysis and the geometrical constraints consideration, the measurement positions are selected. The 5×5 measurement positions are uniformly distributed within $r = 0.2$ to 0.6 m and $z = -0.77$ to -1.05 m on the 270° poloidal plane of VEST. Radial sensor spacing is 10 cm, and vertical sensor spacing is 7 cm. In this case, the interpolation error is predicted to be 3 % for the target magnetic structure.

Four sensors are placed at each measurement positions. Two of the sensors are Hall sensors placed perpendicular to each other. This way the Hall sensors can measure both vertical and toroidal field. The other two sensors are chip inductors that face radial and vertical/toroidal direction. The radial chip inductor can be used as a reference for the radial field to be calculated from vertical field measurements. The vertical/toroidal chip inductor typically measures vertical field, since the slow

varying toroidal field tends to produce only a small and negligible output voltage across the chip inductor ends.

The sensors are soldered closely to each other, so that the distance between the sensors for measurement of a single position is less than 2 cm. Figure 3.3 illustrates the placed sensors. Two printed circuit boards are used to mount and align the sensors. Hall sensors and the vertical/radial chip inductor are aligned with the boards using a jig plate. The boards are glued together in "L" shape to fix the angle between the Hall sensors perpendicular. The precision of the angle between the boards is controlled to 1° using a protractor.
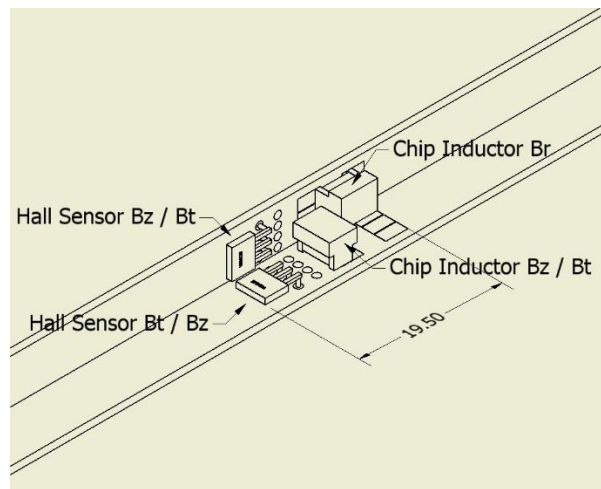
Figure 3.3 Schematic view of the four sensors composing each measurement positions.

3.3 Electromagnetic Interference Consideration

In electronics and telecommunication, the energy transfer takes the form of either conductive, inductive, capacitive, or wave coupling. The undesired transfer of energy is called a noise. In this section, possible sources for each form of noise are discussed. A highlight is laid on the noise in form of wave coupling, or electromagnetic interference (EMI).

Conductively coupled noise is mainly from the power sources. Internal magnetic probe array utilizes a voltage source for Hall sensors. Using the voltage source based on AC-DC conversion, however, tends to introduce the remnants of AC due to the imperfect rectification. Battery is a more reliable voltage source without such AC components. A system of power supply including battery and DC-DC converter is designed for this purpose.

Inductively coupled noise is conventionally the dominant noise source in most plasma diagnostics. A method to deal with such a noise is to twist the signal lines by more than 10 twists per centimeter to reduce the space that might pick up the inductive noise. Special effort to reduce the space between the soldered circuit board site and the sensors. Power lines are also twisted. Twisted pair lines with less number of twists are used for the signal transfer in the region where inductive noise is expected to be small.

Noise by the capacitive coupling rises due to the charge accumulation on the sensor surface from the plasma potential. Normally, the sensors are therefore shielded by sheet metal to compensate for the capacitive noise. A few slits on the sheet metal can suppress the eddy current to avoid any distortion in measurement. For VEST internal magnetic probe array, a copper braided wire is used instead of the sheet metal, which will be explained in detail in the next paragraph.

Electromagnetic wave coupling is the most serious noise source in VEST, where ECH wave of 2.45 GHz is injected for the pre-ionization. The copper braided wire is used to reflect the waves. The small gap between the wires is small compared to the wavelength of the wave, thus reflecting the wave. Moreover, the wire is 10 μm thick and therefore the cutoff frequency due to the skin effect is 42.4 MHz, which is safely between the frequency band of interest, up to 50 kHz, and ECH frequency, 2.45 GHz. Since forming the metal foil of equivalent thickness into cylindrical shape is extremely difficult, the copper braided wire can be a very attractive compensation for the EMI. Figure 3.4 shows the dramatic decrease of ECH wave coupling corrupting the toroidal Hall sensor signal during a plasma discharge. The noise level is on average 9 mV, which is 7 G for Hall sensor and 6 G for chip inductor with integrator with total gain of 20000, for 12 kW ECH power.
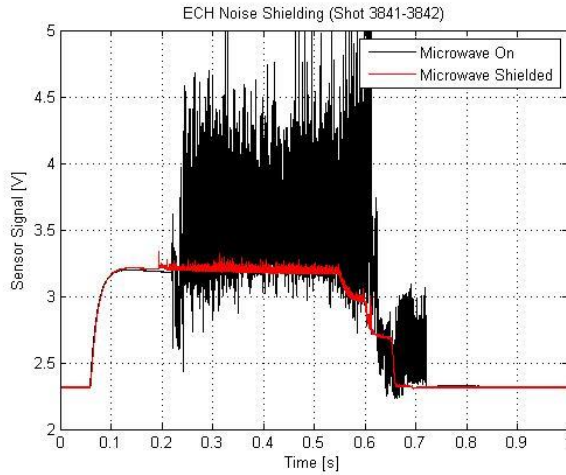
Figure 3.4 Comparison of sensor signal before and after copper braided wire shielding. Red line is the shielded signal, while black line indicates the ECH wave coupling when no shield is used. The measurement is from the separate shots (3841, 3842), and at position $r = 0.3$ m.

Figure 3.4b compares the noise level at $r = 0.2$ m (near the center stack) and $r = 0.6$ m (near the wall). Images from fast CCD camera showed that the $r = 0.2$ m probe is immersed in the plasma for both shots 3841 and 3842, while the $r = 0.6$ m probe is exposed to the direct hit by ECH wave. Therefore Figure 3.4b (a) shows the shielding effect of plasma combined with the copper braided wire, reducing noise level to 4 mV, while Figure 3.4b (b) shows the shielding effect of the copper braided wire only, reducing noise level to mere 61 mV. For Hall sensor, the noise levels are equivalent to (a) 3 G and (b) 47 G. For chip inductor with integrator of gain 20000, the equivalent noise is (a) 2 G and (b) 37 G. It can be concluded that in the case of wall limited plasma, the noise level due to ECH shielded by the copper braided wire is less than 7 G (the level shown in Figure 3.4) for both sensors.
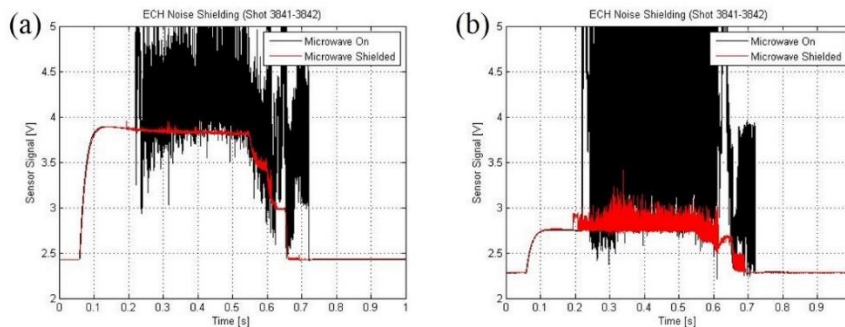
Figure 3.4b Effect of plasma in ECH noise shielding. Position $r = 0.2$ m where plasma covers the probe is shown in (a). Position $r = 0.6$ m where no plasma is present is shown in (b).

Copper braided wire can be understood as a Faraday cage. Since ECH wave tends to leak out of chamber, the part not covered by copper braided wire at the

outside of the vacuum vessel needs a shielding too. Aluminum box is used to complete the Faraday shielding of the probe array. The box thickness is 2 mm and skin effect cutoff frequency is 1.78 kHz. Inductive and capacitive coupling are also shielded by the casing of signal and power lines.

3.4   Thermal Consideration

Thermal load on the magnetic sensors is calculated in Section 3.1. Quartz (fused silica) tube is designed to deal with this thermal load. The tube is also a primary vacuum boundary. In this section, the design of the quartz tube will be discussed.

Materials that can provide the thermal insulation for internal magnetic probes have been studied intensively in the reversed field pinch (RFP) researches [24]. For the RFP heat flux in the scale of GW/m^2, boron nitride or beryllium oxide shows a distinguished performance over the silicon oxide in terms of energy confinement and heat capacity. However, for the VEST heat flux in the scale of MW/m^2 at the upper/lower chamber, the fused silica is a more cost-effective choice. To deal with the elevated heat flux in high current discharges at VEST middle chamber, the future internal magnetic probe array might need another material.

Thickness of the quartz tube is selected considering two factors: the temperature rise and the plasma disturbance. With 1 mm thick quartz tube, the tube outer diameter to 13 mm, the cross sectional area of VEST lower chamber is covered by 10 %. Therefore the quartz tube may not be thicker than 1 mm, to avoid physically disturbing the plasma. On the other hand, energy confinement time is unaffected, since the surface area ratio of the probe array to VEST is only 2.96 %.

Temperature rise is calculated by:

$$Q = c_p m \Delta T \text{ therefore } \Delta T = Q/c_p m \qquad (3.2)$$

Here, c_p is the specific heat of fused silica, 7.4×10^2 J/kg/K, m is the total mass of fused silica calculated by the tube length and thickness and mass density of fused silica, 2.6×10^3 kg/m^3. Q is total incident heat flux.

Surface area of five quartz tubes with outer diameters of 13 mm and lengths of 600 mm is 0.25 m^2. Assuming that the stored energy of 15.9 J (from calculation in Section 3.1) is fully dissipated onto the quartz tubes during the 10 ms discharge, the heat flux density is 6.48 kW/m^2. Then, the temperature rise due to the heat flux is 0.03 ℃.

The temperature rise of 0.03 ℃ will cause a drift of Hall sensor output voltage by 0.14 mV or 0.11 G. Therefore, it can be concluded that no extra cooling channel is required for the internal magnetic probe array in VEST.

Chapter 4 Calibration

4.1   Helmholtz Coil System

To prepare the internal magnetic probe array for actual measurements, there are a few issues that should be resolved. First, fabrication of internal magnetic probe array is done by hands, and therefore erroneous placement of sensors or misalignment of faces are a possibility. Second, the data provided by manufacturer includes a wide tolerance range: 25 % for WSH-135 Hall sensor sensitivity and 15 % for 1812CS-XGLC chip inductor effective area. Third, the temperature drift in Hall sensor output requires exact sensitivity value for given ambient temperature measured to the 1 °C. Finally, the frequency response of the sensors is not known; only the bandwidth is provided by the manufacturer. All these issues can be resolved by an absolute calibration of the magnetic sensors.

Helmholtz coil is a branch of the solenoid-type magnetic field source that generates a more uniform field inside the coil then does a solenoid. A pair of coils with radius R is placed with distance R and connected in series as shown in Figure 4.1.
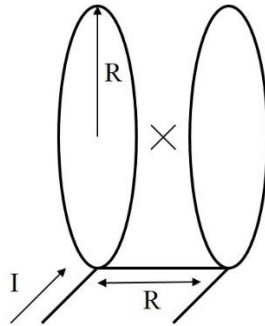
Figure 4.1 Illustration of Helmholtz coil pair. Marked by a cross is the center of the coil..

The magnetic field inside the coil, as shown in Equation 4.1, is simply a superposition of the fields from each coils that can be calculated by Biot-Savart law.

$$B(r) = \frac{\mu_0 n I}{R} \frac{1}{\pi \sqrt{Q}} \left[E(k) \frac{1 - \alpha^2 - \beta^2}{Q - 4\alpha} + K(k) \right] \qquad (4.1)$$

Here, r is the radial distance from the Helmholtz coil axis, $R = 0.03$ m (3 cm) the coil radius, I the coil current, and $n = 14$ the number of turns for each coils. $K(k)$

and $E(k)$ are the complete elliptic integrals of first and second kinds, respectively, for $k = (4\alpha/Q)^{1/2}$ and $Q = [(1+\alpha)^2 + \beta^2]$ where $\alpha = r/R$ and $\beta = 1/2$. Derivation of this relation is not described in this thesis.

The designed Helmholtz coil is 3 cm in radius, 14 turns for each coils, and yields 4.2 G per current of 1 A at the center of the coil. Wire of diameter 1.02 mm featuring the current limit of 83 A for 10 seconds (18 in American Wire Gauge) is used. The uniformity of the field in the center of the Helmholtz coil is shown in the Figure 4.2. The field structure is confirmed by a Tesla meter. Typically, 23 A of current is used to produce the averaged central magnetic field of 100 G at the central region where the sensors are situated.

Figure 4.2 Calculated magnetic field generated in a Helmholtz coil. Solid lines mark the 100 G and 0.5 cm.

The current source for the Helmholtz coil is explained in the next section. The current flowing in the Helmholtz coil is monitored by a Pearson coil. A Pearson coil is a non-contact current measurement device that encircles the wire and measures the magnetic field generated by the current. The model used here converts 1 A into 0.1 V. The voltage signal is monitored by an oscilloscope.

Alignment of the sensors inside the Helmholtz coil is done by a successive adjustment of sensor face direction with several test shots prior to the actual calibration discharge. When the sensor face is perfectly aligned with the magnetic field, the output voltage becomes maximum. Calibration discharge is done at such a perfectly aligned situation.

4.1.1 Power Supply for Helmholtz Coil

A function generator is used to generate the oscillating power, which then turns into the oscillating magnetic field by a Helmholtz coil. The required current for the production of 100 G magnetic field at the center is 23 A. With Helmholtz coil dc resistance being 1.2 Ω, the required voltage is 27.6 V and the required power is 634.8 W. Common function generators do not supply such a large power.

An audio amplifier is used to produce the oscillation in phase with the pulse of a function generator, amplified to the desired power level. Audio amplifiers are ideal for the application to VEST magnetic sensor calibrations, since the frequency band of interest in VEST research is similar to the audible frequency band. Gain of 34 dB (× 50) allows a burst of 1 V peak voltage to be amplified to 42 A and 2.08 kW for the resistive load Helmholtz coil. Eurofer © amplifier EP4000, featuring the power limit of 4 kW, is used.

4.2   Sensitivity Calibration

Magnetic sensors are absolutely calibrated by Helmholtz coil in the frequency range of 0.03 ~ 50 kHz and the magnetic field of ~ 100 G. The two factors to be calibrated is the sensitivity and the phase shift. Assuming the sinusoidal oscillation of magnetic field $B = B_0 \sin\theta$ and the sensor signal $U = U_0 \sin(\theta + \varphi)$, sensitivity K and phase shift φ can be calculated as follows.

$$K(f) = U_{max}/B_{max} \qquad\qquad (4.2a)$$

$$\varphi(f) = \cos^{-1}\left[\langle U \cdot B\rangle / \sqrt{\langle U^2\rangle \cdot \langle B^2\rangle}\right] \qquad (4.2b)$$

Here, $K(f)$ is the sensitivity, U_{max} and B_{max} the maximum sensor voltage and magnetic field respectively, and $\varphi(f)$ the phase shift in degrees.

Sensitivities of the sensors taking into account the errors from fabrication and temperature drift are determined by the absolute calibration. Table 4.1 shows the exact sensitivities of all sensors after fabrication. Positions are denoted by both a letter (for vertical position where a rod is placed) and a number (for radial position of the sensor within a rod). All values of sensitivity are obtained for 100 G magnetic field oscillating at 1 kHz when ambient temperature is 20 ℃. Units of the values are V/T for Hall sensors and cm^2 for chip inductors. The values are different from part to part, but within ± 2.5 V/T for Hall sensor and within 0.60 cm^2 for chip inductor.

Table 4.1 Absolute sensitivities of the sensors. Positions are described by a letter and a number. Units for Hall sensor is V/T, and units for chip inductor is cm^2.

Position	Hall sensor B_t	Hall sensor B_z	Chip inductor B_t	Chip inductor B_r
A1	12.22	13.49	7.77	7.18
A2	13.94	12.80	7.74	7.25
A3	13.28	12.92	7.14	7.70
A4	13.11	13.41	7.09	7.52
A5	10.95	11.74	7.55	7.37
B1	13.85	13.53	8.12	7.96
B2	13.97	13.34	7.36	7.66
B3	13.64	13.75	7.66	7.61
B4	13.18	12.17	7.21	8.07
B5	13.61	12.45	7.86	7.29
C1	13.68	13.35	7.25	7.87
C2	13.36	12.97	7.56	7.86
C3	12.21	13.10	7.80	7.41
C4	13.95	10.71	8.03	7.64
C5	13.58	10.46	8.12	7.03
D1	13.06	13.65	7.61	7.01
D2	12.96	12.57	7.11	7.59
D3	12.47	13.05	7.12	7.90
D4	12.51	13.43	7.26	8.09
D5	13.15	12.79	7.97	7.10
E1	13.12	13.25	7.25	7.64
E2	13.02	13.00	7.94	7.52
E3	12.51	13.04	7.24	6.95
E4	13.58	13.20	7.37	7.35
E5	13.41	14.05	7.21	7.14

Typical waveform of Helmholtz coil current is compared with the signals from both of the sensors in Figure 4.3. The current monitored by a Pearson coil is converted to the magnetic field shown in the figure. The signal from chip inductor is numerically integrated using trapezoidal rule. Signals from both sensors are converted into magnetic fields using the sensitivity values of Table 4.1. It can be observed that the three waveforms are in seamless agreement. The position of the sensors is E3.
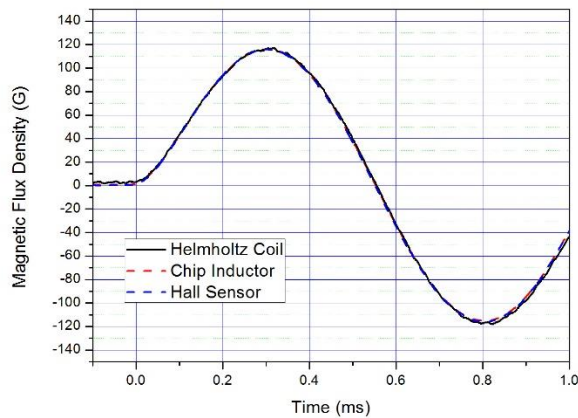
Figure 4.3 Typical responses of sensors to the Helmholtz coil magnetic field: The magnetic field from Helmholtz coil (black line), chip inductor (red dashed line) and Hall sensor (blue dashed line).

The frequency response of the magnetic sensors show similar tendencies from part to part. Therefore, the result from the sensors at position E3 is shown as a representative in Figure 4.4. It can be observed from the figure that Hall sensor sensitivity decreases significantly at 30 kHz. It can be said that from 0.03 kHz up to 10 kHz, Hall sensor data can be processed using the sensitivity value on Table 4.1. Chip inductor effective area has a flat response down to 100 Hz, but a large drop of the effective are is observed at 50 Hz. The signal level is smaller than the noise level at 50 Hz, so the effective area evaluation loses the reliability. From the observations, it can be said that the two sensors may be used for different frequency bands, which will be elaborated in the next paragraph. Use of an analog integrator with 1 ms time constant and additional gain of 10 (total gain of 10000) for a single channel of chip inductor signals showed an integrated sensitivity of 7.52 V/T for the chip inductor with calibrated effective area of 7.52 cm^2, as expected.
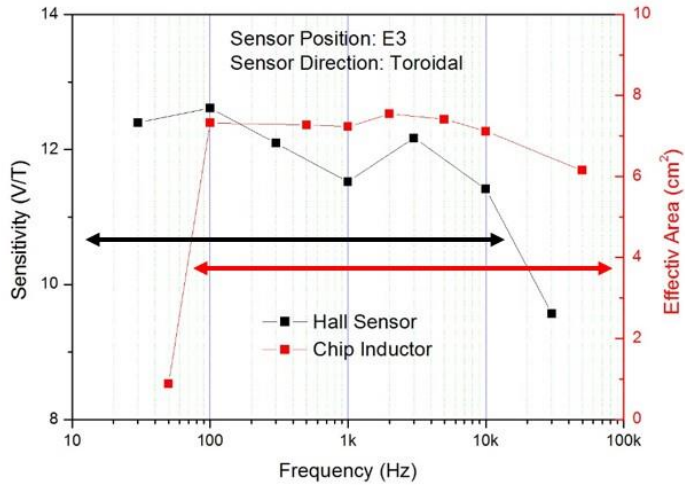
Figure 4.4 Sensitivity and effective area during frequency scan in Helmholtz coil for a Hall sensor (black) and a chip inductor (red), respectively. The region reliable operation is marked by arrows of corresponding colors.

Arrows in Figure 4.4 represents the bandwidth of each sensors, showing an important characteristic of the internal magnetic probe array. As summarized on Table 4.2, the frequency band of Hall sensor and chip inductor is different. Chip inductor covers the higher frequency band from 100 Hz up, and Hall sensor covers the lower frequency band from 10 kHz down. Therefore at the frequency band from DC to 100 Hz, Hall sensor is more reliable; at the frequency band from 10 kHz to 50 kHz, chip inductor will be used more dominantly. At the Intermediate frequency band from 100 Hz to 10 kHz where both sensors are reliable, cross-check of both sensors can be done. The enhanced reliability is enjoyed in this band, owing to the redundancy of measurements.

Table 4.2 Summary of calibration results using Helmholtz coil. Chip inductor result is shown in the value when the analog integrator is used.

	Hall sensor	Chip inductor
Sensitivity	13 V/T ± 2.5 V/T	7.52 V/T ± 0.6 V/T
Frequency band	DC ~ 10 kHz	100 Hz ~ 50 kHz

4.2.1 Copper Braided Shielding Effect

Metallic sheets that are commonly adopted to suppress the charge build-up on the magnetic sensor surfaces affects the measurement due to the skin effect. The

material and thickness determines the level of distortion by the relation:

$$\delta = \sqrt{\frac{2\rho}{\varpi\mu}} \qquad (4.3)$$

Here, the e-folding depth, or skin depth δ, is related to the resistivity of conductor ρ, the angular frequency of current ω, and the absolute magnetic permeability of the conductor μ.

In VEST, copper braided wire is used as a shield for EMI and capacitive noise, which are normally suppressed using the sheet metal. The main advantage of using the copper braided wire instead is that it is composed of extremely thin wires with diameter as small as 10 μm. The skin effect cutoff frequency, where the oscillation amplitude is reduced by 1/e, is 42.4 MHz in this case. The phase shift is plotted in Figure 4.5, and shows negligible phase shift in the frequency range below 50 kHz, consistent with the prediction. Figure 4.3 also shows the negligible phase delay among the sensors and the Helmholtz coil.
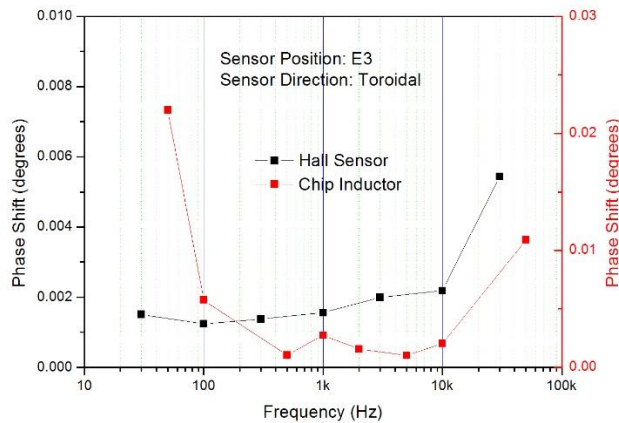
Figure 4.5 Phase shift during the frequency scan in Helmholtz coil for a Hall sensor (black) and a chip inductor (red). Note the scale of phase shift is below 0.1 ° for both sensors.

Chapter 5 Installation and In-situ Calibration on VEST

5.1   System Assembly

The designed, fabricated and calibrated internal magnetic probe array can be assembled and installed on VEST. In this section, an overview of the installation process of the internal magnetic probe array is described with photos.

Printed circuit boards are glued perpendicularly and mounted with sensors as shown in Figure 5.1. The image is best understood by comparison with Figure 3.3. Some idle soldering sights can be seen in the photo, mounted by none of the sensors. These sites are originally for the Christmas light bulbs, since the commercially available circuit boards are used. The conducting traces of the boards are scratched-out to modify the circuit to avoid any unwanted couplings.
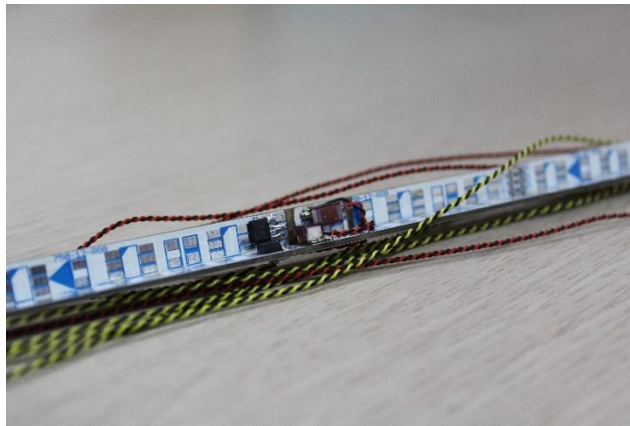
Figure 5.1 Image of fabricated circuit board with sensor mount.

An assembly of a circuit board with sensors is shown in Figure 5.2a. Five such rods constitute the internal magnetic probe array. It can be seen in the photo that the signal lines are connected to 50-pin connector, which transfers the signal to twisted pair shielded lines and to the digitizer. Figure 5.2 also shows a steering rod, which allows mechanical adjustment of the rod alignment. Section 5.2.1 describes the process of mechanical alignment in detail. Figure 5.2b shows a part of the copper braided wire, and the small rings linking the steering rod to the main printed circuit board assembly.
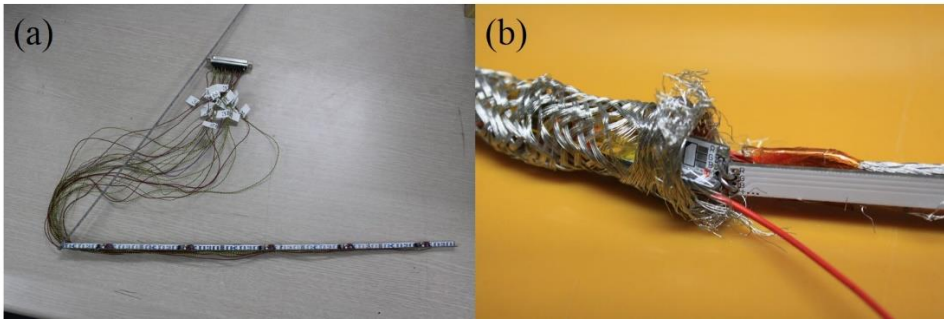
Figure 5.2 Image of a circuit board – sensor assembly. (a) An overview and (b) a zoomed view of copper braided wire end and steering rod – main board link.

Quartz tube with one end closed houses the circuit board – sensor assembly. The inner diameter is 11 mm, which is enough to house the 7 mm wide and 1 mm thick circuit boards glued perpendicularly[1]. Small gap of 0.4 mm is left, actually, and the rods tend to rotate inside the tube. Length of the quartz tube is 600 mm, to cover from $r = 0.2$ to 0.8 m, safely passing the vacuum vessel wall at $r = 0.6$ m.

Quick-disconnect structure, or Wilson's seal, is used to hold the quartz tube. Wilson's seal is in essence two rubber O-rings separated by a plastic ring. The rubbers provide a mechanical isolation by elasticity. Figure 5.3 shows the internal magnetic probe array being installed. Three quick-disconnect structures out of five are shown in the figure. Also shown in the photo is a topless aluminum box. An aluminum duct is used as the box. The duct is used because it is abundant in the lab and easy to be opened and closed using the prescribed groove structure.

Figure 5.3 Image of internal magnetic probe array being installed, seen from the outside of the vacuum vessel.

---

[1] Diagonal length is 10.6 mm = $\{(7 \text{ mm})^2 + (7 + 1 \text{ mm})^2\}^{1/2}$ by Pythagoras's rule.

Figure 5.4 shows the installed internal magnetic probe array seen from the inside of the VEST vacuum vessel. Kapton tape is used as an electrical insulator between the sensors mounted on the printed circuit boards, and the copper braided wire. The copper braided wire is not shown in the photo.
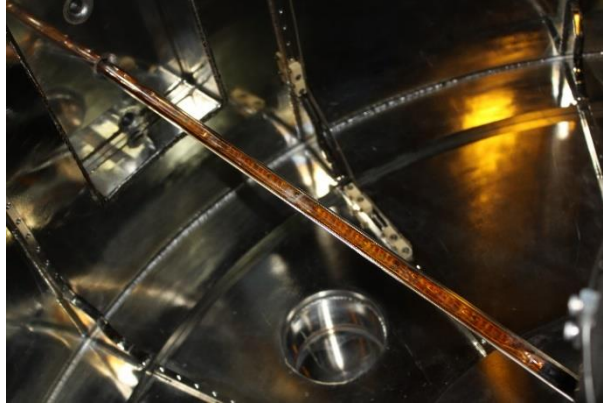
Figure 5.4 Image of internal magnetic probe array being installed, seen from the inside of the vacuum vessel.

Overview of the full 5×5 internal magnetic probe array is shown in Figure 5.5 schematically. The installed magnetic probe array is highlighted by the red box. The ratio of the lower chamber poloidal cross sectional area (z = -1.2 to -0.6 m) to the probe array surface area (0.013 m × 5) is 10.8 %.
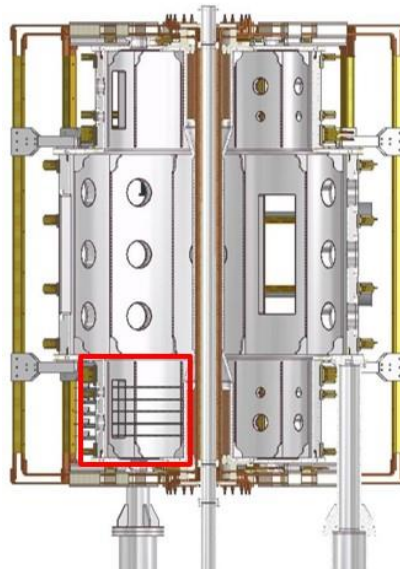
Figure 5.4 Cutaway view of VEST with the internal magnetic probe array (red box).

5.2   In-situ Calibration

The process of installation introduces additional errors to the measurement. Misalignment of the sensor with the desired field direction is a serious problem. A new method for the compensation of this tilted angle, inspired by the idea of UTST, [25] is described in Section 5.2.1. Another problem introduced by installation process is that the measurement position cannot be guaranteed, since the installed probe array is not visible during the shots. The novel way of in-situ calibration for this problem is suggested in Section 5.2.2.

5.2.1   Tilted Angle

Rotation of the rod inside the quartz tube creates a misalignment of the mounted magnetic sensors to the fields to be measured. Assuming the tilted angle θ, the measured field strength is related to the actual field strength by:

$$B_\varphi = \widetilde{B_\varphi} \cos \theta + \widetilde{B_z} \sin \theta \qquad (5.1a)$$

$$B_z = -\widetilde{B_\varphi} \sin \theta + \widetilde{B_z} \cos \theta \qquad (5.1b)$$

Here, the magnetic field components marked with tilde are measured fields, and those without mark are actual fields.
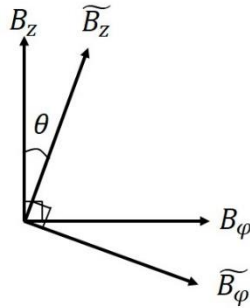
Figure 5.6 Illustration of tilted angle in-situ calibration. Compare with Equation 5.1.

Using the Equation 5.1, the actual magnetic field can be calculated once the tilted angle θ is known and the measured magnetic fields are given. To obtain the θ, the toroidal field can be used. With poloidal field coils turned off, left hand side of Equation 5.1b is zero, and tilted angle θ can be calculated by:

$$\theta = \tan^{-1} \frac{\widetilde{B_z}}{\widetilde{B_\varphi}}. \qquad (5.2)$$

Equation 5.1a may be not relevant in this calculation, since real B_φ is not known as exactly as the real B_z.

Every VEST shot includes a large time domain when only the toroidal field is applied. This domain may be used for the in-situ tilted angle calibration. An example of the in-situ calibration is shown in Figure 5.7. Red line is the measured vertical field signal corrupted by toroidal field crosstalk, and black line is the real vertical field calculated by Equation 5.1, using θ measured during the time domain 200 ~ 300 ms. It is seen that toroidal field crosstalk in the sensor facing vertical field can be subtracted completely after the application of the linear relations (Equation 5.1) with θ calibrated using in the aforementioned time domain.
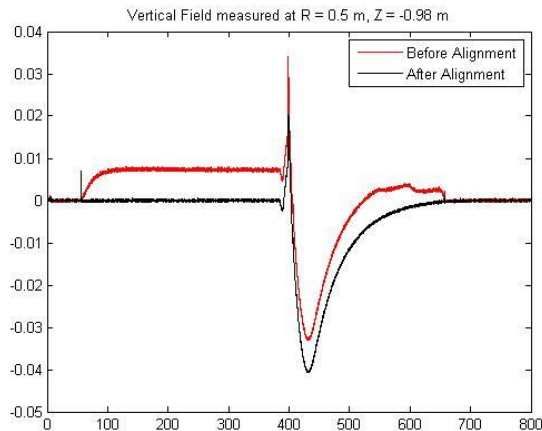
Figure 5.7 In-situ calibration of tilted angle during a shot. X axis is time in millisecond, and Y axis is magnetic field in Tesla. Red line is the measured vertical field signal corrupted by toroidal field crosstalk, and black line is the real vertical field calculated by Equation 5.1, using θ measured during time domain 200~300 ms.

5.2.2　Position

The installed internal magnetic probe array cannot be monitored visually. This means the exact radial positions of the sensors are difficult to know. To deal with this problem, a new calibration method is suggested. This method is made available since the measurement of steady toroidal field is easy with Hall sensor, unlike in the conventional pickup-coil based measurements. In conventional magnetic probe

measurements, the toroidal field component is commonly suppressed by the high pass filters.

Toroidal field of a tokamak is inversely proportional to major radius, since the coils around the torus are more closely spaced at the inboard side than are at the outboard side. In VEST, the so-called $1/R$ dependence of toroidal field strength is verified with shot-to-shot progressive insertion of a single magnetic probe. By monitoring the toroidal field coil current, an exact toroidal field at a given radial position is known. Therefore, the toroidal field can be an in-situ source of absolute calibration for radial probe position. Figure 5.8 shows the prototype internal magnetic probe[2] that is used for the scan of toroidal field. The toroidal field of 0.1 T is generated on axis at R = 0.4 m by 8.3 kA toroidal field coil current.

Figure 5.8 Image of the prototype of the internal magnetic probe array.

The procedure of the calibration is explained in this paragraph. Toroidal field discharge is recorded by the Hall sensors. Tilted angle calibration is done to correct the misalignment in direction. Then the measured values are compared with the known toroidal field strength, calculated directly from the monitored toroidal field coil current. If those two values disagree, either the physical sensor position or the position used in calculation is changed until the two values agree.

One example of the calibration is shown in Figure 5.9. Designed measurement positions are r = 0.20, 0.30, 0.40, 0.50 and 0.60 m, but the comparison shown in Figure 5.9 (a) shows the disagreement between the measured and calculated fields. Since the measured toroidal field is bigger, it can be assumed that actual position of the sensors are located to the inboard side a little bit.

Assuming the probe positions are shifted 2 cm to the inboard side, toroidal fields are recalculated, as shown in Figure 5.9 (b). The plot shows good agreement.

---

[1] The large pickup coil is adopted with Hall sensor for cross-reference. Dimension of the probe is 3 cm in every direction. Stainless steel tube holds the probes.

It can be concluded that the Hall sensors are placed at $r = 0.18, 0.28, 0.38, 0.48$ and 0.58 m. Chip inductor positions can be calibrated from their relative positions to Hall sensors. This method of calibration is applicable to any tokamak as an in-situ calibration means of magnetic sensors, when toroidal field can be measured accurately.
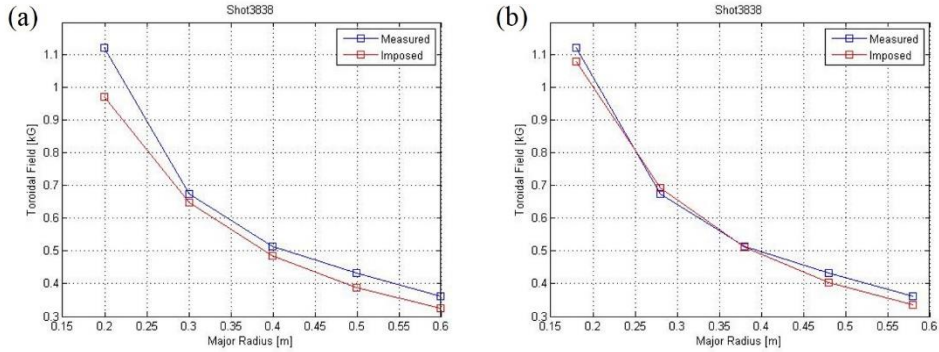

Figure 5.9 Comparison of measured toroidal field (blue) and calculated toroidal field (red). Comparisons before (a) and after (b) calibration are shown.

Chapter 6 Test Experiments on VEST

6.1 Vacuum Field Measurements

In the previous sections, the design, fabrication, installation, and calibrations of the internal magnetic probe array are discussed. The internal magnetic probe array can now be used for the actual measurement.

VEST is being prepared for a unique startup scheme using partial solenoids, to address the issue of startup in spherical tokamak. To envisage the inspiration, the magnetic field structure generated by a partial solenoid should be measured. From the knowledge of absolute values of the partial solenoid field, the operation scenario of other coils can be designed. In this section, application of the internal magnetic probe array to vacuum field measurements is discussed.

6.1.1   Experimental Setup

Partial solenoid, like other poloidal field coils installed in VEST, is driven by a double swing circuit of a capacitor bank. A swing down of PF2 (the partial solenoid) generates an average field varying typically within $\pm$ 160 G, during the 4 ms swing down period. Sensor voltage output is then expected to be 192 mV and 121 mV for Hall sensor and chip inductor, respectively. Assuming the noise level to be 5 mV, the signal-to-noise ratio of the sensors are 38 and 24, respectively. Therefore, both of the sensors can be used for the vacuum field measurement.

Radial field component can be derived from the measurement of vertical fields. *The code* is a numerical software for such a process. This code is tested with *the simulation*, which is another numerical software that calculates the flux function from both the monitored actual current in PF2 coil and the predicted eddy currents at the vessel walls. Equation 1.1 in Section 1.2 shows the relation between the flux function and the source current density.

The validity of *the code* should be tested before it can be used in processing the actual measurements. Calculations from *the simulation* is used as a test-bed. First, the vertical field components at the 5×5 measurement positions calculated from *the simulation* are assumed to be known. The fields at intermediate positions are then interpolated subsequently in radial and vertical directions by cubic spline

method with natural end condition, with grid sizes of 1 mm. Then, the interpolated vertical fields are radially integrated by trapezoidal rule. Here, the integration constants are assumed to be the boundary flux functions, which are assumed to be known. The resulting flux functions are compared with the test flux functions. The comparison shows *the code*'s feasibility in reproducing the flux function from the exact measurement of vertical field. The result is shown in Figure 6.1a, where it can be observed that the error is negligible.

Figure 6.1a Comparison of flux function reconstructed by *the code* (red) and *the simulation* (black). Each subplots are time evolution of flux function in Weber at the specific positions within the measurement range.

Next, the flux function derived from *the code* is differentiated in vertical direction by Lagrange interpolation using 3 points. The derivative is proportional to the local radial field. Then the radial field from the code can be compared with the radial field from the simulation. The result is shown in Figure 6.1b. The Lagrange interpolation is represented by:

$$f_j' = \frac{-3f_j + 4f_{j+1} - 2f_{j+2}}{2h} + O(h^2) \qquad (6.1)$$

Here, f_j' is the derivative at j, f_j, f_{j+1} and f_{j+2} the known points at the corresponding positions, and *h* the uniform grid size of 1 mm.
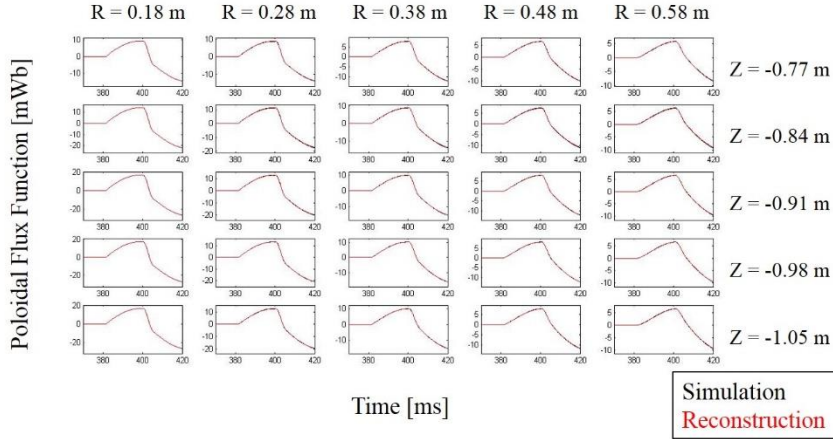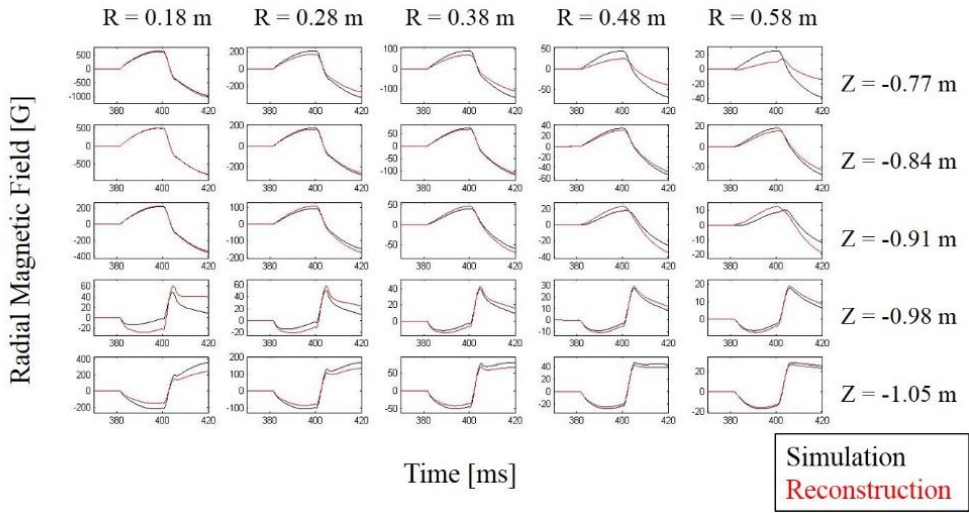
Figure 6.1b Comparison of radial field reconstructed by *the code* (red) and *the simulation* (black). Each subplots are time evolution of radial field in Tesla at the specific positions within the measurement range. Notice the disagreement in some of the positions.

Figure 6.1b shows a general agreement between *the simulation* and *the code*, but disagreements occur at boundaries. The maximum error is 64 G (17.85 %) at R = 0.18 m and Z = -1.05 m, and average error is 4 G (6.72 %). It can be concluded that the code itself introduces an error of 4 G on average. Near the boundary, the error tends to be bigger.

6.1.2   Result and Discussion

In the previous section, the numerical error introduced by *the code* is found to be 4 G. Now the actual measurements are processed with *the code*. If the measurement were accurate, the error would be no more than 4 G on average.

The vacuum field measured by the internal magnetic probe array is shown in Figure 6.2. Both sensors showed similar results. Time of the plot is t = 400 ms, when the current in PF2 coil is positive (to the inside of the paper), and therefore the direction of field is clockwise by the right-hand rule. It can be observed from Figure 6.2 that the vertical field lines pour out of the top (z = -0.8 m) of PF2 heading towards the bottom (z = -1.1 m) of PF2, as expected. More detailed comparison is discussed in the following paragraphs.
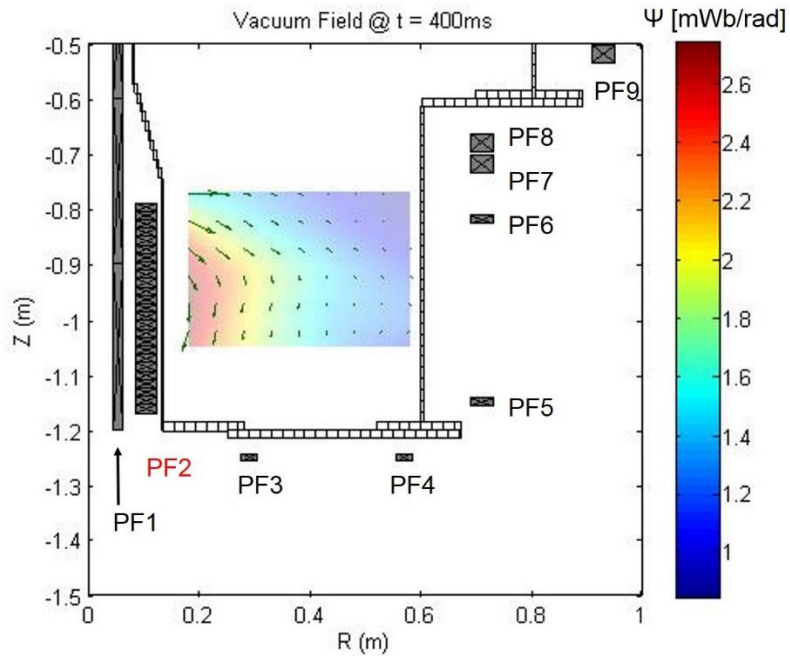
Figure 6.2 Vacuum field measurement from shot 3835 at t = 400 ms. Colored surface is flux function, and vector is poloidal magnetic field. Partial solenoid or PF2 is marked with red name. Positive current flows into the paper.

In this measurement, the vertical field measurement at two of the 25 points were replaced with *the simulation* due to the malfunction of the toroidal magnetic sensors at both positions. Without toroidal magnetic sensors, the tilted angle cannot be determined and it is unable to subtract the toroidal field crosstalk from the poloidal field measurement.

Time evolution of PF2 coil current is shown in Figure 6.2b. Pearson coil is used for the measurement. A positive current of +0.8 kA is observed at t = 400 ms.
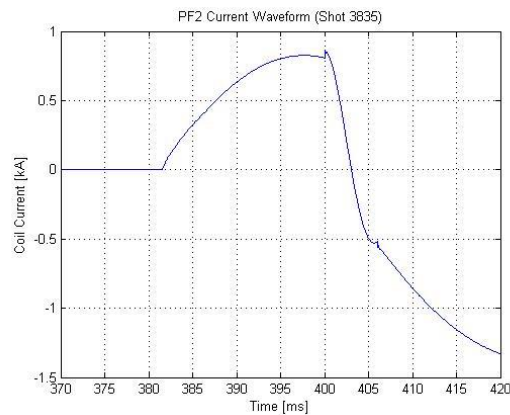
Figure 6.2b Time evolution of actual PF2 coil current monitored during shot 3835.

The detailed comparison of the results are shown in Figure 6.3. At the center of the measurement region, eddy currents from wall has little effect and therefore prediction of field is easy. Figure 6.3 (a) shows that the measurement agrees well with *the simulation* in this region. Near the boundary of the chamber, the eddy current is hard to predict due to the complex geometry of the vacuum vessel walls. Figure 6.3 (b) shows the disagreement of the measurement with *the simulation*. Through the modification of the wall modeling parameters, this disagreement may be reduced. Both Figures 6.3 (a) and (b) shows the noise level of the measurement, which is below 1 G, or 1.3 mV.

Figure 6.3 Comparison of measured magnetic field (red) and simulated magnetic field (black) (a) at the center and (b) near the vacuum vessel during shot 3835.

6.2 Phantom Plasma Field Measurement

Experiments with vacuum field can be concluded that the internal magnetic probe array measures the vacuum field accurately in many positions, except for some positions at the edge where the eddy current modelling is rather difficult. In this section, ability of the internal magnetic probe array to reconstruct the current d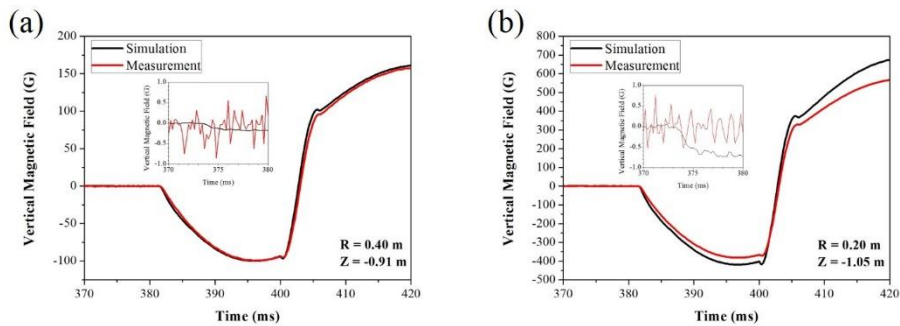ensity profile is tested. Time evolution up to 50 kHz is expected to be measured accurately (see Section 4.2), so if the plasma current can be measured at a specific time, the evolution of the plasma current can be measured.

Plasma current at VEST using partial solenoid is less than 1 kA, and a stable scenario to generate such a plasma is yet under development. Therefore, the actual demonstration of current distribution measurement is not possible at the moment. In this situation, a phantom plasma can be used as a test-bed for the ability to reconstruct a plasma current density profile from the internal magnetic probe array measurement.

6.2.1   Experimental Setup

A phantom plasma is a numerically assumed spatial distribution of plasma current density. A simple bell-shaped distribution is used.

$$J_\varphi(r,z) = J_{\varphi,0}(1 - (d/a)^2)^k \qquad (6.2)$$

Here, $J_{\varphi,0}$ is the factor that fixes the total current to a specific value I_p:

$$J_{\varphi,0} = \frac{I_p}{\int J_\varphi(r,z)dS} \qquad (6.2b)$$

and d is the distance between the prescribed plasma center and the position (r, z):

$$d = \sqrt{(r - R_0)^2 + (z - Z_0)^2} \qquad (6.2c)$$

where a is the plasma radius, and k the so-called peakedness factor. With Equations 6.2, magnetic fields can again be calculated from Equation 1.1.

For a phantom with total plasma current 5 kA, plasma radius 0.15 m and peakedness 2, magnetic field in the range of ± 120 G is generated. The signal to noise ratio is 17 and 10 for Hall sensor and chip inductor with integrator gain of 20000, respectively, assuming the noise level of 9 mV based on the measurement shown in Figure 3.4 (Section 3.3). In the actual measurement, the magnetic field

from external coils will be superimposed to the magnetic field by plasma current, and the signal to noise ratio will be improved. However, only the magnetic field by the phantom plasma is considered in this section.

Typical phantom discharge is shown in Figure 6.4. Peak current density is 0.239 MA/m^2 at magnetic axis at $r_0 = 0.4$ m and $z_0 = 0.9$ m. A grid of 61×41 points with 1 cm grid size within $r = 0.2 \sim 0.6$ m and $z = 0.6 \sim 1.2$ m is used to calculate the magnetic structure from the phantom current.
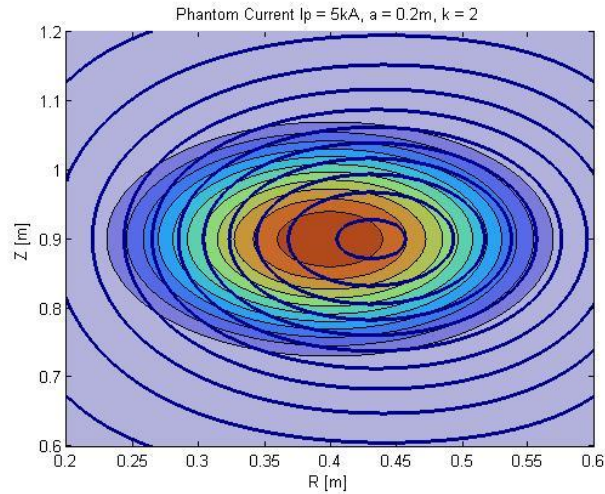
Figure 6.4 Typical phantom plasma. Color denotes the current density and line denotes the contour of the flux function.

Local current density is related to the vertical and radial field by Equation 2.7a. The ability of *the code* to reconstruct the current density from the poloidal field components is tested and shown in Figure 6.5. The figure shows the comparison between reconstructed current density and the phantom current at $z_0 = 0.9$ m. The reconstruction is done directly with the magnetic fields calculated from the phantom current distribution, with no interpolation. The error is negligible, and it remains low even if the 7 G of random noise is included to the measured vertical field. Using Hall sensor, the noise level of 7 G occurs when ECH wave is shielded by plasma and the copper braided wire, as shown in Figure 3.4. In case of chip inductor, the noise level is 6 G.

Figure 6.5 Test result of reconstruction of the current density from the local poloidal magnetic field. The reconstructed current (red) agrees with the phantom current (black).

6.2.2　Result and Discussion

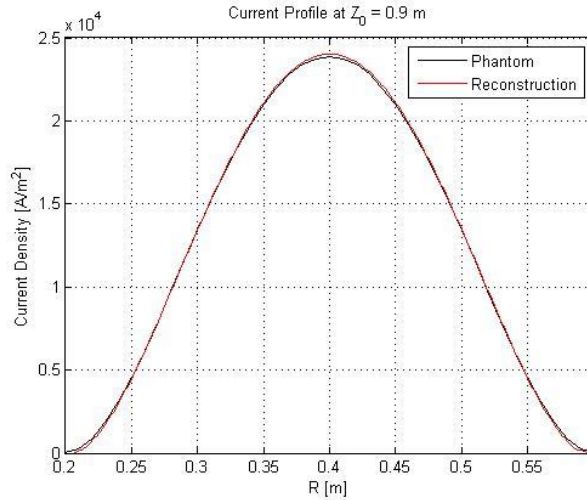With the ability of *the code* to reconstruct the current density profile validated in the previous section, the actual measurement of various plasma shapes are tested. In this section, the plasma shape will be changed, thus changing the gradient scale length of the vertical magnetic field (which is measured). Then the vertical field is assumed to be known, and used in reconstruction of the radial field, and subsequently of the current density. Comparing this reconstructed value with the prescribed phantom current will reveal the feasibility of the internal magnetic probe array in measurement of said plasma shape. The vertical component of the phantom plasma field is assumed to be measured at 25 points where the sensors of the internal magnetic probe array are actually installed. The measurement error of no more than 7 G is randomly added to the initial vertical field data.

Figure 6.6 shows the reconstruction result of the phantom plasma current with total current of 5 kA within radius $a = 0.2$ m and peakedness $k = 2$. The gradient scale length of the vertical field produced by this plasma is 3.02 cm. In this case, the numerical interpolation, integration and differentiation gave rise to a 0.35 kA/m^2 error in peak current density (1.45 %). It can be said that the radial spacing of 10 cm is adequate to measure a magnetic field gradient scale length of 3 cm through cubic spline interpolation.

48

Figure 6.6 Comparison of phantom current profile (black) with the expected measurement result (red) at $Z_0 = 0.9$ m, in the case of plasma current 5 kA, plasma radius 0.2 m, and peakedness $k = 2$.

Another phantom plasma is devised to establish a relation between the gradient scale length and the feasibility of the probe array. Figure 6.7a shows the variation of Figure 6.6 case with increased peakedness of $k = 4$. Gradient scale length of the field in this case is 2.33 cm. The increased peakedness of a phantom plasma leads to the decrease in scale length of the field variation. Interpolation error increases due to the inability to reproduce the variation of fields between the interpolation points. Error of peak current density increased due to the interpolation error to -3.58 kA/m^2, or -8.74 %. Overall shape of a plasma is reconstructed to be relaxed, because the steep gradient of magnetic field cannot be interpolated accurately with such a coarse grid of 10 cm.
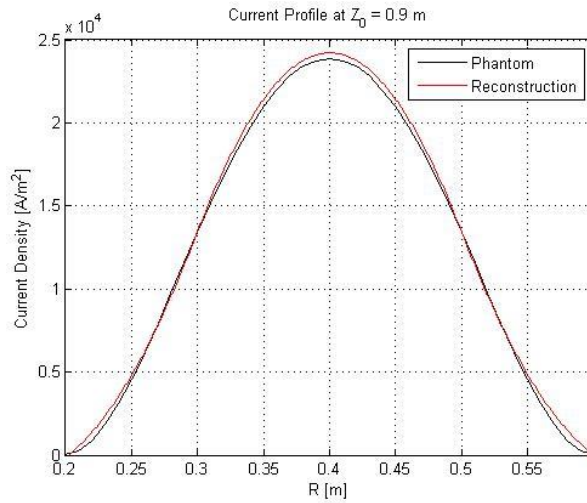
Figure 6.7a Comparison of phantom current profile (black) with the expected measurement result (red) at $Z_0 = 0.9$ m, in the case of plasma current 5 kA, plasma radius 0.2 m, and peakedness $k = 4$.

Another possible phantom plasma is that with more relaxed shape. Figure 6.7b shows a phantom plasma current density profile with peakedness of $k = 1$, with the other parameters and noise level identical to the case of Figure 6.6. Gradient scale length of the field generated by the plasma is 3.82 cm. The decreased peakedness of a phantom plasma leads to the increase in the scale length of the field variation. Figure 6.7b shows the reconstruction error. The peak position is shifted because of the measurement noise. Also, the reconstructed plasma shape is steeper than the phantom plasma, which suggests that inclusion of wiggles during interpolation led to unwantedly steep field gradient. The wiggles are observed when interpolation grid is too small for the variation of the targeted variation. The error in peak current density is 4.21 kA/m^2 or 5.24 %.
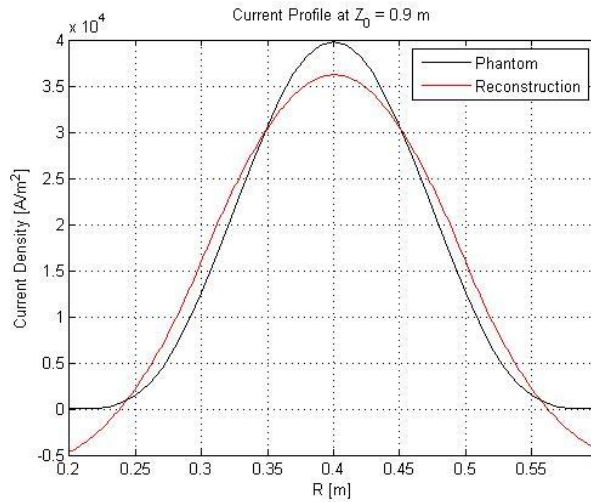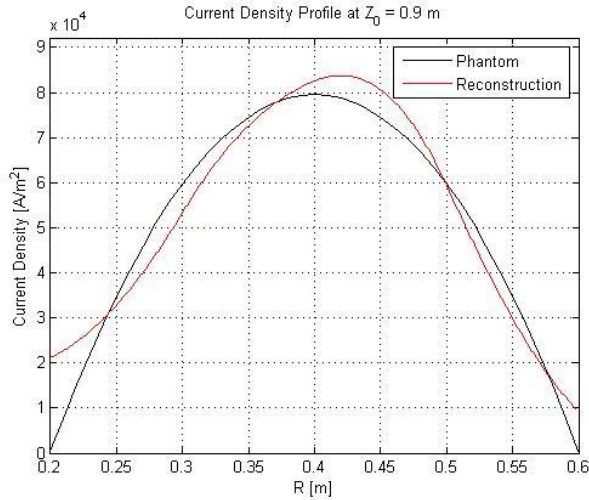
Figure 6.7b Comparison of phantom current profile (black) with the expected measurement result (red) at $Z_0 = 0.9$ m, in the case of plasma current 5 kA, plasma radius 0.2 m, and peakedness $k = 1$.

It can now be concluded from the set of experiments that the gradient scale length and the spacing between sensors has an optimum match when the measurement grid size is 10 cm, whereas the gradient scale length is 3 cm. With 2.33 cm scale length, the error was -8.74 %. While the 3.82 cm scale length caused +5.24 % error. If the gradient scale length is shorter than the measurement grid, the error is introduced by the inaccurate representation of the field structure between the measurement positions. On the other hand, long gradient scale length causes the slight wiggle in interpolation process, thus increasing the error. The current internal magnetic probe array measures the field with gradient scale length of 3 cm with best accuracy of less than 2 %.

Chapter 7 Conclusion

7.1　Summary and Conclusion

The work described in this thesis deals with the development of internal magnetic probe array with dual sensor in VEST. In this section, summary of the thesis is presented with some emphasis on the important chapters.

A partial solenoid structure of VEST made the vacuum field measurement important. Equally important is the measurement of plasma merging, which means the internal magnetic probe should cover a wide range of frequency. Two types of sensors, Hall sensor and chip inductor, are used to achieve this objective.

System is therefore designed focusing on two points. First, adoption of dual sensors is maintained. Second, the size is maintained as small as possible. Frequency band and sensitivity of sensors are selected carefully. Electromagnetic interference and thermal load is considered.

Calibration of the sensors were performed for extended bandwidth of 30 Hz to 50 kHz. Methods of in-situ calibration after the installation are suggested, using the known toroidal field of VEST. Misalignment angle and measurement positions can be absolutely calibrated prior to each measurements in VEST.

Test experiments on the measurement of vacuum field and phantom plasma field is performed. Vacuum field produced by partial solenoid is measured and may provide the reference to the modelling of eddy current in the vessel wall. The plasma current that generates vertical field gradient scale length of 3 cm is evaluated to be measured with less than 2 % accuracy using the current design of internal magnetic probe array.

It can be concluded that the thesis provides a design reference for the internal magnetic probe array with Hall sensor and chip inductor that can measure the wide frequency range. With the results from the test experiments, it can also be concluded that the developed internal magnetic probe array is ready for the startup phase of VEST.

7.2   Future Work

Future work on can largely be in three ways. One, the method of determining the boundary flux function should be developed. In this thesis, the calculated flux function is used instead of actual measurement. One idea of the actual measurement is to use the signal of flux loops already installed in VEST. Installation of additional pickup coil on the center stack may also provide the boundary flux function more directly.

Second work remaining is the adjustment of the interval of the probe array. Radial interval may increase by soldering additional sensor clusters on the sites pointed by the red arrows in Figure 7.1, or a new printed circuit board may be designed to allow an easier adjustment of the sensor intervals. Non-uniform grid may also contribute to the enhanced accuracy in reconstruction of a current density profile.
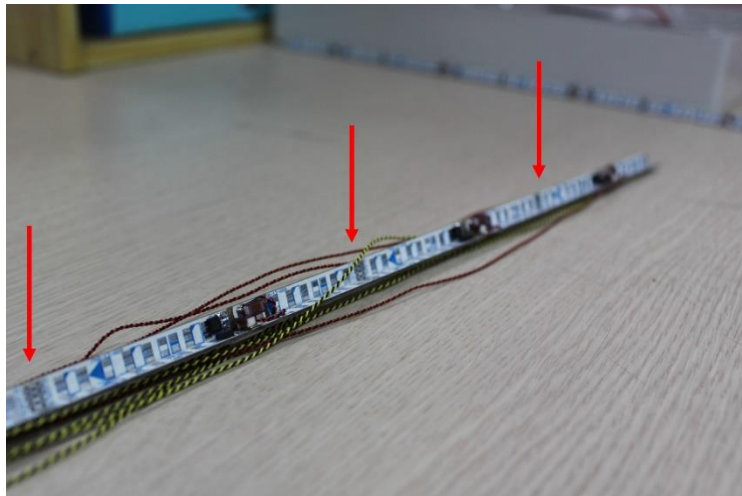
Figure 7.1 Image of one of the rods mounted with three sensor clusters. The sites pointed by the red arrows are available for soldering of additional clusters. With the sites occupied the radial interval becomes 5 cm, rather than the current 10 cm.

Finally, the middle chamber magnetic probe array should be developed. The renewed heat load calculation and target magnetic structure assessment is required. Probe material and cooling channels are should be considered. Middle chamber discharge may include phenomena with wider range of frequency, so chip inductors with smaller inductance, therefore featuring larger L/R cutoff frequency, may be needed. New source of calibration with higher frequency capability is then required. Engineering problems such as the limited size of rectangular flange should be resolved, for example by holding the probe array with a stack attached to the wall.

Bibliography

[1] Y.-K.M. Peng, *The Physics of Spherical Torus Plasmas,* Physics of Plasmas, 2000. 7: p. 1681

[2] A. Sykes, E. del Bosco, R.J. Colchin, G. Cunningham, D. Duck, T. Edlington, D.H.J. Goodall, M.P. Gryaznevich, J. Holt, J. Hugill, J. Li, S.J. Manhood, B.J. Parham, D.C. Robinson, T.N. Todd, and M.F. Turner, *First Results from the START Experiment,* Nuclear Fusion, 1992. 32: p. 694

[3] Sykes, A., R.J. Akers, L.C. Appel, E.R. Arendsa, P.G. Carolan, N.J. Conway, G.F. Counsell, G. Cunningham, A. Dnestrovskijb, Yu.N. Dnestrovskijb, A.R. Field, S.J. Fielding, M.P. Gryaznevich, S. Korsholmc, E. Lairdd, R. Martin, M.P.S. Nightingale, C.M. Roach, M.R. Tournianski, M.J. Walshe, C.D. Warrick, H.R.Wilson, S. You, MAST Team, and NBI Team, *First Results from MAST,* Nuclear Fusion, 2001. 41: p. 1423

[4] K.J. Chung, Y.H. An, B.K. Jung, H.Y. Lee, J.J. Dang, J.W. Lee, J. Yang, J.G. Jo, D.H. Choi, Y.G. Kim, Y.S. Na, and Y.S. Hwang, *Initial Plasma Start-up Using Partial Solenoid Coils in Versatile Experiment Spherical Torus (VEST),* Fusion Engineering and Design, 2013. To be published.

[5] L.L. Lao, H. St. John, R.D. Stambaugh, A.G. Kellman, and W. Pfeiffer, *Reconstruction of Current Profile Parameters and Plasma Shapes in Tokamaks,* Nuclear Fusion, 1985. 25: p. 1611

[6] Y.S. Hwang, C.B. Forest, D.S. Darrow, G. Greene, and M. Ono, *Reconstruction of Current Density Distributions in the CDX-U Tokamak,* Review of Scientific Instruments, 1992. 63: p. 4747

[7] L.L. Lao, J.R. Ferron, R.J. Groebner, W. Howl, H. St. John, E.J. Strait, and T.S. Taylor, *Equilibrium Analysis of Current Profiles in Tokamaks,* Nuclear Fusion, 1990. 30: p. 1035

[8] W.F. Bergerson, P.Xu, J.H. Irby, D.L. Brower, W.X. Ding, and E.S. Marmar, *Far-infrared Polarimetry Diagnostic for Measurement of Internal Magnetic Field Dynamics and Fluctuations in the C-MOD Tokamak,* Review of Scientific Instruments, 2012. 83: p. 10E316

[9] Y. Zhou, Z.C. Deng, Y.G. Li, and J. Yi, *Multi-channel Far-infrared HL-2A Interferometer-polarimeter,* Review of Scientific Instruments, 2012, 83: 10E336

[10] D.M. Thomas, A.W. Leonard, R.J. Groebner, and T.H. Osborne, T.A. Casper, P.B. Snyder and L.L. Lao, *Measurement of Edge Currents in DIII-D and their Implication for Pedestal Stability,* Physics of Plasmas, 2005. 12: p. 056123

[11] F.M. Levinton, G.M. Gammel, R. Kaita, H.W. Kugel, and D.W. Roberts, *Magnetic Field Pitch Angle Diagnostic using the Motional Stark Effect,* Review of Scientific Instruments, 1990. 61: p. 2914

[12] I.H. Hutchinson, *Principles of Plasma Diagnostics,* Second Edition, 2002: Cambridge University Press

[13] J. Lee, K.J. Chung, Y.H. An, J. Yang, Y.G. Kim, B.K. Jung, Y.S. Hwang, T.S. Hahm, and Y.S. Na, *Design and Commissioning of Magnetic Diagnostics in VEST,* Fusion Engineering and Design, 2013. To be Published.

[14] D.L. Bowers, B.S. Liley, A.H. Morton, and C.F. Vance, *A Slow Toroidal θ-Z Pinch Experiment,* Plasma Physics, 1971. 13: p. 849

[15] I.H. Hutchinson, *Magnetic Probe Investigation of the Disruptive Instability in Tokamak LT-3,* Physical Review Letters, 1976. 37: p. 338

[16] L. Giannone, R.C. Cross, and I.H. Hutchinson, *Internal Magnetic Probe Measurements of MHD Activity and Current Profiles in a Tokamak,* Nuclear Fusion, 1987. 27: p. 2085

[17] C.A. Romero-Talamás, P.M. Bellan, and S.C. Hsu, *Multielement Magnetic Probe using Commercial Chip Inductors,* Review of Scientific Instruments, 2004. 75: p. 2664

[18] I. Ďuran, J. Stöckel, G. Mank, K. H. Finken, G. Fuchs, and G. Van Oost, *Measurement of Magnetic Field Fluctuations using an Array of Hall Detectors on the TEXTOR Tokamak,* Review of Scientific Instruments, 2002. 73: p. 3482

[19] Y. Liu, D.A. Maurer, G.A. Navratil, and N. Rivera, *High Spatial Resolution Hall Sensor Array for Edge Plasma Magnetic Field Measurements,* Review of Scientific Instruments, 2005. 76: p. 093501

[20] I. Ďuran, O. Hronová, J. Stöckel, J. Sentkerestiová, and J. Havlicek, *Magnetic Measurements using Array of Integrated Hall Sensors on the CASTOR Tokamak,* Review of Scientific Instruments, 2008. 79: p. 10F123

[21] I. Ďuran, J. Sentkerestiová, K. Kovarik, and L. Viererbl, *Prospects of Steady State Magnetic Diagnostic of Fusion Reactors based on Metallic Hall Sensors,* AIP Conference Proceedings, 2012. 1442: p. 317

[22] M. Ariola, and A. Pironti, *Magnetic Control of Tokamak Plasmas,* 2012: Springer

[23] Winson ⓒ , Linear Hall Effect Sensor IC WSH-135 (Datasheet)

[24] J.T. Slough, and K.E. Miller, *Small, High Frequency Probe for Internal Magnetic Field Measurements in High Temperature Plasmas,* Review of Scientific Instruments, 2001. 72: p. 417

[25] R. Imazawa, M. Nakagawa, S. Kamio, R. Hihara, T. Yamada, M. Inomoto, Y. Takase, and Y. Ono, *First Plasma Experiment on Spherical Tokamak Device UTST,* Electrical Engineering in Japan, 2012. 179: p. 20

국 문 초 록

시동 단계의 VEST에서 자기장 널 (Null) 구조와 플라즈마 병합 과정을 위시한 자기장 구조를 측정하기 위해 내부 자기장 탐침 시스템이 개발되었다. 느리거나 빠르게 변하는 자기장을 모두 측정할 수 있도록 홀 센서와 칩 인덕터의 두 가지 측정기가 사용되었다. 측정기의 크기가 작기 때문에, 자기장 탐침 시스템이 플라즈마 변수를 심각하게 변화시키지 않으면서도 플라즈마로 삽입될 수 있다.

세라믹 코어 칩 인덕터와 집적 홀 센서가 측정기로서 선택되었다. 선택 과정에서는 노이즈 이상의 최소 측정 가능 자기장과 주파수에 따른 영향이 고려되었다. 그 후 목표하는 자기장 구조를 조사하여 내삽 오차를 최소화하면서도 공학적 한계에 부합하는 25개의 측정 지점이 확정되었다. 측정기들은 그 위치의 특수 설계된 기판 위에 3방향을 측정할 수 있도록 납땜되었다. 다양한 전자기 간섭 현상이 방호되었고 특히 편조선을 이용하여 전자 자기 공명 주파수 마이크로파 노이즈를 7 G로 줄였다. 플라즈마 에너지로부터의 열 부하가 계산되어 쿼츠 관의 설계에 참고하였다. 섭씨 0.2도의 온도 상승이 예측되었기 때문에 별도의 냉각 계통은 구성하지 않았다.

측정기들은 설치가 완료된 후 헬름홀츠 코일을 이용해 절대적으로 보정되었다. 100 G의 자기장을 낼 전력을 공급하기 위해 오디오 앰프가 이용되었다. 홀 센서의 감도는 13 V/T이며 주파수 반응은 0.03부터 10 kHz이다. 칩 인덕터 감도는 7.52 V/T이며 주파수 반응은 0.1부터 50 kHz까지이다. 두 감지기의 위상 편이는 편조선을 사용했음에도 무시할 만했는데, 이는 편조선이 매우 얇은 금속판처럼 취급될 수 있기 때문이다.

보정된 자기 측정기는 VEST 아래쪽 챔버에 설치되었다. 측정기들의 정렬 문제는 VEST의 토로이달 자장을 이용해 바로 보정되었다. 반지름 방향으로의 측정기 위치 역시 토로이달 자장을 이용해 보정되었다. 이

보정 방법들은 토로이달 자장이 정확히 측정될 수 있기에 제안될 수 있었음을 주목할 만 하다.

시험 측정은 진공 자기장을 이용해 진행되었다. 챔버 중앙에서 측정된 진공 자기장은 예상된 바와 잘 일치하였다. 그러나, 가장자리에서는 맴돌이 전류를 예상하기 어렵기 때문으로 보이는 불일치가 관찰되었다. 또 다른 시험 측정은 수치적으로 펼쳐진 플라즈마 전류에 대해 수행되어 플라즈마 병합시 내부 자기장 탐침 시스템의 사용 가능성을 증명하고자 했다. 현재의 설계로는 수직 방향 자기장 변화의 특성 길이가 3 cm인 플라즈마 전류 분포에 대해 2 % 이하의 오차로 측정할 수 있음을 알 수 있었다.

Flux function의 재구성 방법은 내부 자기장 탐침을 플럭스 루프나 픽업 코일과 혼용하여 개선될 수 있다. 측정기간의 간격은 좀더 다양한 플라즈마 모양을 재구성할 수 있도록 업그레이드될 수 있다. 이상의 경험들을 바탕으로, 가운데 챔버에 적합한 내부 자기장 탐침 시스템이 가까운 미래에 개발될 수 있다.